

Contents lists available at ScienceDirect

Journal of Volcanology and Geothermal Research

journal homepage: www.elsevier.com/locate/jvolgeores



Invited review article

Seismic perspectives from the western U.S. on magma reservoirs underlying large silicic calderas



Brandon Schmandt ^{a,*}, Chengxin Jiang ^b, Jamie Farrell ^c

- ^a University of New Mexico, Department of Earth and Planetary Sciences, Albuquerque, NM 87131, USA
- ^b Harvard University, Department of Earth and Planetary Sciences, Cambridge, MA 02138. USA
- ^c University of Utah, Department of Geology and Geophysics, Salt Lake City, UT 84112, USA

ARTICLE INFO

Article history: Received 29 April 2019 Received in revised form 11 July 2019 Accepted 17 July 2019 Available online 24 July 2019

Keywords: Silicic caldera Magma reservoir Seismic tomography Sill complex

ABSTRACT

Since 1.25 Ma, three volcanic systems in the western U.S. Cordillera hosted rhyolitic eruptions of ≥300 km³ dense rock equivalent creating the Yellowstone (0.63 Ma), Long Valley (0.76 Ma), and Valles (1.25 Ma) calderas. Their similar time scales since caldera-forming eruptions and rich histories of seismic research motivate a review of seismic constraints on the modern magma reservoirs beneath these calderas from the uppermost mantle to the upper crust. Across the Cordillera upper mantle seismic velocities are generally below the continental average and each of the calderas is underlain by exceptionally low velocities consistent with the presence of mantle melt, ≲3%. Concentrated upper mantle low-velocity anomalies are found beneath the eastern Snake River plain southwest of Yellowstone caldera and beneath Long Valley caldera. Valles caldera is located above a broadly distributed low-velocity anomaly associated with the Rio Grande Rift and Jemez volcanic lineament. At lower crustal depths potential magma reservoirs exhibit weaker seismic velocity anomalies and greater variability among the results of different tomographic inversion methods compared to shallower depths. At middle-to-upper crustal depths, ~5–15 km, seismic tomography provides evidence of magmatic reservoirs beneath all three calderas, and scattered wave imaging supports sharp upper, lateral, and/or lower boundaries of each inferred magma reservoir. Estimates of average melt fractions in these reservoirs vary from ~9-23% based on recent tomography, with localized melt fraction estimates as high as ~30-60% based on sharp interfaces detected by scattering and ray bending analyses. The wide range of inferred melt fractions likely results from contrasting sensitivities of different seismic imaging methods combined with spatially heterogeneous melt fractions and uncertainties in mapping seismic velocities to silicate melt fractions. Seismic radial anisotropy beneath Yellowstone and Long Valley calderas indicates that middle-to-upper crustal reservoirs are organized as sill complexes with relatively crystalpoor and crystal-rich layers, suggesting magma storage in many weakly connected volumes. Future estimates of (an)isotropic seismic velocities and melt fractions across 3D reservoirs may be improved through expanded applications of full waveform tomography to body and surface waves and increasingly dense array studies facilitated by combinations of broadband and rapidly-deployable shorter-period seismographs. Advanced seismic imaging offers potential for improved delineation of magma reservoir boundaries and constraints on intrareservoir structures such as sill complexes that provide insight into magma reservoir mechanics and compositional heterogeneity.

© 2019 Elsevier B.V. All rights reserved.

Contents

1.	Introd	uction	159
2.	Tector	nic and volcanic background	159
	2.1.	Yellowstone caldera	161
	2.2.	Long Valley caldera	162
	2.3.	Valles caldera	162
3.	Metho	ds for seismic imaging of crustal and upper mantle magmatic systems	162
	3.1.	Body wave tomography	162
	3.2.	Surface wave tomography	163

E-mail address: bschmandt@unm.edu (B. Schmandt).

Corresponding author.

	3.3.	Natural source scattered wave imaging	63
4.	Seism	ic imaging constraints	64
	4.1.	Upper mantle melt	64
	4.2.	Lower crustal magma reservoirs	65
	4.3.	Middle-to-upper crustal reservoirs	66
	4.4.	Seismically anisotropic magma reservoirs	69
	4.5.	Uncertainty in seismic signatures of crustal magma	70
5.	Integr	ated magmatic system structure and links to volcanic life cycles	72
	5.1.	Potential origins of continued mantle melt supply	72
	5.2.	Multi-stage crustal reservoirs	72
	5.3.	Links to prior rhyolitic magma reservoirs and volcanic life-cycles	72
6.	Summ	ary and future opportunities	73
Ackı	nowledg	gements	74
Refe	rences		74

1. Introduction

Voluminous silicic magmatic systems carry out the fundamental geological process of using primitive mantle melts as thermal and compositional inputs to derive felsic igneous rocks in the continental crust (Bachmann and Huber, 2016). They also fuel highly explosive calderaforming eruptions that yield voluminous ignimbrites, continentalscale ashfalls, and potentially global atmospheric effects (Cashman and Giordano, 2014; Newhall et al., 2018; Timmreck, 2012). The intensity and duration of global climate and ecological effects of large explosive eruptions are debated (e.g., Woltering et al., 2011; Lane et al., 2013; Smith et al., 2018). However, even the largest historical eruption of ~50 km³ dense-rock-equivalent (DRE) from Tambora volcano in 1815 C.E. produced widespread environmental effects that would be increasingly problematic for the growing global human population (Oppenheimer, 2003; Newhall et al., 2018). The estimated global recurrence interval of eruptions with a volcanic explosivity index (VEI) >7 (Newhall and Self, 1982), which corresponds to eruptions of ≥40 km³ DRE, is ~1000 years (Pyle, 1995; Deligne et al., 2010; Rougier et al., 2018). The potential impact of explosive caldera-forming eruptions and the relevance of the underlying systems to fundamental questions about magma transport and differentiation motivate efforts to constrain the current state of large silicic magmatic systems (Pritchard and Gregg, 2016; Bachmann and Huber, 2016).

Compared to magmatic systems that fuel less voluminous and compositionally evolved eruptions, silicic caldera-forming magmatic systems may provide especially tractable targets for subsurface geophysical imaging methods like seismology. Such magmatic systems must episodically accumulate large volumes of magma that have undergone major compositional evolution within the crust, consequently these systems are likely to have prominent effects on lithospheric seismic structure. This review focuses on three modern magmatic systems in the western U.S. that underlie large silicic calderas and attempts to synthesize seismic constraints on the presence, geometry, and internal properties of their modern magma reservoirs from the upper mantle to the upper crust.

Yellowstone, Long Valley, and Valles calderas are located in the western U.S. Cordillera and each formed as a consequence of a VEI ≥ 7 Quaternary eruption (Crosweller et al., 2012). Their most recent caldera-forming rhyolitic eruptions and corresponding DRE volumes are: the 0.63 Ma Lava Creek tuff-forming eruption of ~1000 km³ DRE at Yellowstone caldera (Matthews et al., 2015; Christiansen, 2001), the 0.76 Ma Bishop tuff-forming eruption of ~650 km³ DRE at Long Valley caldera (Andersen et al., 2017; Hildreth and Wilson, 2007), and the 1.25 Ma Upper Bandelier tuff-forming eruption of ~350 km³ DRE at Valles caldera (Phillips et al., 2007; Heiken et al., 1990). The eruptions that formed Yellowstone and Long Valley calderas are classified as VEI 8 eruptions, but characteristics of the eruption that formed Valles caldera place it near the VEI 7–8 boundary with a minimum volcanic magnitude estimate of 7.8 (Pyle, 2015; Crosweller et al., 2012). Geophysical

evidence supports the presence of modern magmatic systems beneath all three calderas; although, the amount of magma, spatial distribution of magma, and life-cycle stage of each system are debated.

Key to this review is that studies of the three western U.S. volcanic systems mentioned above benefit from an extensive history of localto-continental scale seismograph deployments. Local seismic networks from long-term monitoring networks and temporary experiments constrain the crustal structure at each site. The local scale seismic arrays are complemented by the recent availability of continuous broadband seismic sampling across the western U.S. from the Transportable Array (TA) component of EarthScope's USArray (earthscope.org). The continuous ~70-km spacing of the TA recently bolstered opportunities for deeper seismic imaging and inter-regional comparison. Sub-caldera magmatic systems in the western U.S. were the focus of some pioneering threedimensional (3D) seismic tomography studies of continental magmatic systems (Benz and Smith, 1984; Kissling, 1988; Ankeny et al., 1986). Increasingly advanced isotropic and anisotropic seismic imaging studies were subsequently enabled by methods including 3D ray tracing (Weiland et al., 1995), joint tomographic inversions of local and teleseismic data (Huang et al., 2015), scattered wave migration (Aprea et al., 2002; Nakata and Shelly, 2018), ambient noise seismic interferometry (Stachnik et al., 2008; Seats and Lawrence, 2014; Jiang et al., 2018a), and full waveform tomography (Flinders et al., 2018).

Given the three systems' broadly similar erupted compositions, erupted volumes, and time scales since caldera formation combined with the rich history of seismic investigations, we consider questions about how their underlying structures reflect the fundamental aspects of voluminous silicic magmatic systems and the life-cycle stages of these specific systems: Is there ongoing mantle melt supply at any or all three systems? Does magma accumulate in one or more reservoirs and do those reservoirs occur at similar depth intervals beneath each caldera? How much magma is present and how does it compare with past eruptive reservoirs? What are the internal properties of magma reservoirs in the crust? Updated insights regarding these questions have emerged from modern seismic imaging studies interpreted in the context of recent advances in other geophysical, geochemical, and geological studies of large silicic magmatic systems.

2. Tectonic and volcanic background

Each of the three magmatic systems has a distinctive regional tectonic setting, none of which is in the modern volcanic arc fueled by the Cascadia subduction zone (Fig. 1). Only Yellowstone is part of a clear hotspot-style spatiotemporal progression of rhyolitic caldera forming volcanism and it has geophysical and geochemical indications of a deep mantle plume source (Smith et al., 2009; Pierce and Morgan, 2009; Obrebski et al., 2010; Schmandt et al., 2012; Nelson and Grand, 2018; Camp and Ross, 2004; Graham et al., 2009). Among the simplest indications of deep upwelling beneath Yellowstone is the radially symmetric geoid that is centered on the caldera (Fig. 2C). It is the most

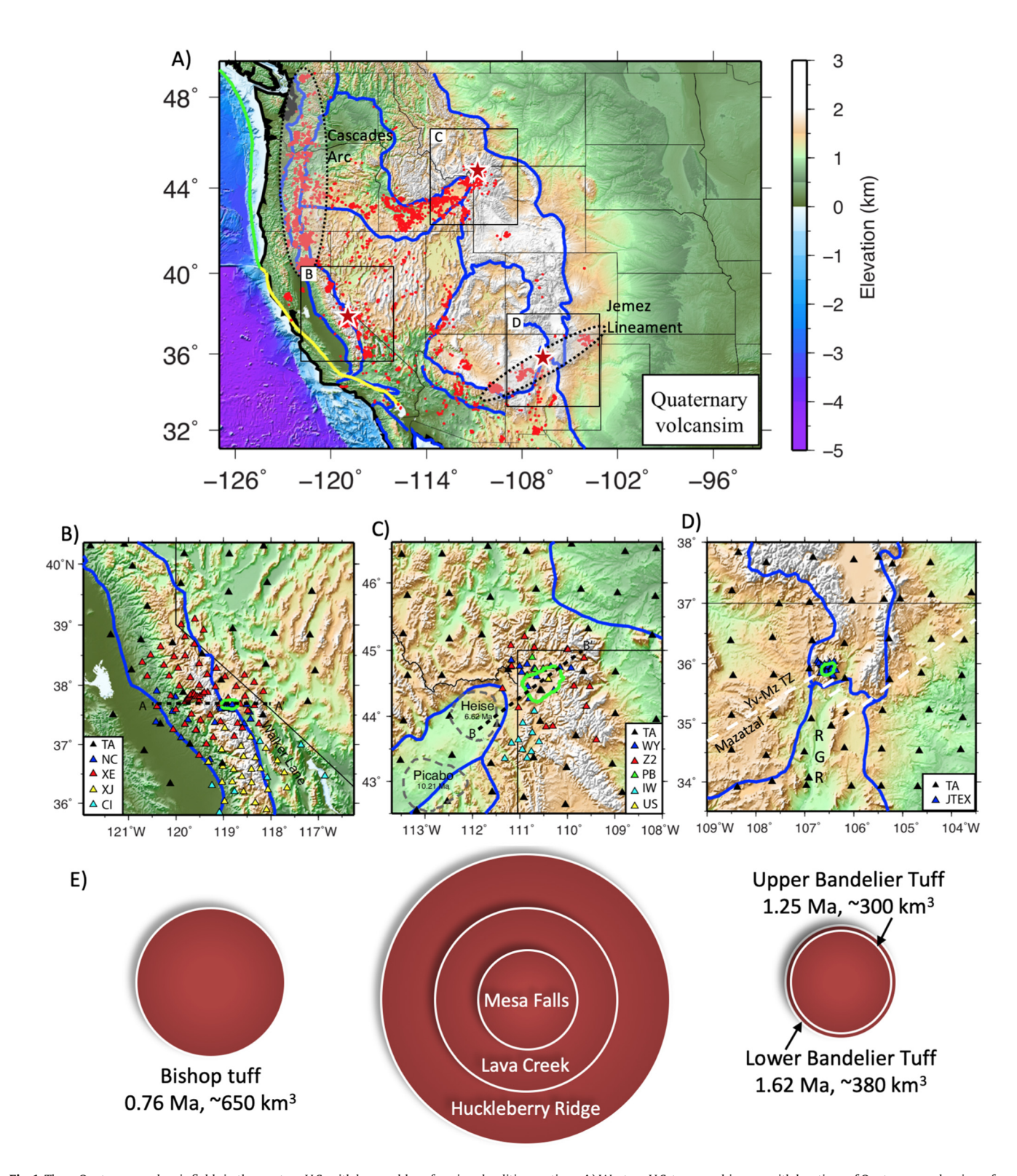


Fig. 1. Three Quaternary volcanic fields in the western U.S. with large caldera-forming rhyolitic eruptions. A) Western U.S. topographic map with locations of Quaternary volcanism of any composition in red dots (Walker et al., 2004) and the locations of the Yellowstone, Long Valley, and Valles calderas labeled with red stars. Physiographic province boundaries of the Cordillera (Fenneman, 1917) and the San Andreas transform and Cascadia subduction zone plate boundaries are labeled. Subduction-driven volcanism of the Cascades arc and the Jemez Lineament volcanic regions are enclosed by dashed black contours. B-D) Seismic networks used for imaging the crust and upper mantle beneath Long Valley, Yellowstone (modified from Jiang et al., 2018a), and Valles calderas (Steck et al., 1998; Aprea et al., 2002), respectively. The TA stations are shown for all three regions because they are the primary data source for shallow upper mantle imaging, but they were not used for local imaging at Valles caldera presented in Fig. 7. A smaller scale map showing the JTEX stations at Valles caldera used by Aprea et al. (2002) is provided in Fig. 7D. E) Rhyolitic eruption volumes are represented assuming discs of unit thickness scaled to show the relative volumes of silicic tuffs from caldera-forming events. Estimated dates and DRE eruptive volumes are labeled for Long Valley and Valles calderas (Andersen et al., 2017; Hildreth and Wilson, 2007) and Valles caldera (Phillips et al., 2007; Cook et al., 2016; Crosweller et al., 2012). The ages and volumes for the three Yellowstone eruptions are: the 2.08 Ma and ~2500 km³ Huckleberry Ridge tuff, the 1.3 Ma and ~280 km³ Mesa Falls tuff, and the 0.63 Ma and ~1000 km³ Lava Creek tuff (Christiansen, 2001; Rivera et al., 2014, 2016; Matthews et al., 2015).

prominent geoid anomaly in the western U.S., which indicates anomalously deep buoyancy. However, it should be noted that there continues to be sufficient evidence to motivate alternative hypotheses for the origin of the Yellowstone hotspot that do not require a mantle plume (Christiansen et al., 2002; James et al., 2011; Leonard and Liu, 2016; Zhou et al., 2018; Zhou, 2018). Evaluating the importance of plume and non-plume mantle sources is not a goal of this review. Here, the focus is the magmatic system from the shallow upper mantle (<100 km) to the upper crust, which corresponds to the depth interval from where most primitive melts form up to where voluminous rhyolites typically accumulate prior to caldera-forming eruptions (Cashman and Giordano, 2014; Bachmann and Huber, 2016). Thus, the regional tectonic settings that influence stress and strain in the lithosphere and the history of large eruptions are considered key background for the following review of seismic constraints on magmatic system structure.

2.1. Yellowstone caldera

The Yellowstone hotspot track is defined by a sequence of rhyolitic caldera complexes that decrease in age from ~16 Ma to 0.63 Ma over ~800 km from southwest to northeast (Armstrong et al., 1975; Smith and Braile, 1994; Matthews et al., 2015). Northeast propagation of magmatism started near the western edge of Precambrian North America, formed the Snake River plain province, and continued into the Archean Wyoming craton where the Yellowstone caldera resides

(Armstrong et al., 1975; Anders and Sleep, 1992; Pierce and Morgan, 2009). Basaltic volcanism continues in the wake of the rhyolitic calderas (e.g., Potter et al., 2019), with eruptions as young as ~2100 years B.P. on the eastern Snake River Plain (Kuntz et al., 2007). Miocene initiation of the Yellowstone hotspot was approximately coincident with the beginning of orogenic collapse that formed the Basin and Range province. The transition to an extensional state of stress is associated with growth of the Pacific-North America transform boundary at the expense of the former subduction zone margin (Atwater, 1970; Dickinson and Snyder, 1979; Schellart et al., 2010) and possibly the arrival of the Yellowstone plume (Colgan and Henry, 2009; Camp et al., 2015). The current regional state of stress in the lithosphere surrounding the Yellowstone caldera is thought to be organized by a deep source of buoyancy beneath the hotspot and cooling and subsidence in the wake of the hotspot, which results in ongoing southwest extension across the Yellowstone plateau constrained by geodesy (Fig. 2D; Lowry et al., 2000; Puskas et al., 2007; Kreemer et al., 2014).

Three rhyolitic caldera-forming eruptions have occurred at the Yellowstone hotspot's current caldera complex (Crosweller et al., 2012). The first and largest was the Huckleberry Ridge tuff-forming eruption of ~2500 km³ DRE at 2.08 Ma (Christiansen, 2001; Rivera et al., 2014; Singer et al., 2014). It was followed by the Mesa Falls tuff-forming eruption of ~280 km³ DRE at 1.3 Ma (Christiansen, 2001; Rivera et al., 2016) and the Lava Creek tuff-forming eruption of ~1000 km³ DRE at 0.63 Ma (Christiansen, 2001; Matthews et al., 2015). Since the 0.63 Ma eruption, a sequence of rhyolitic eruptions occurred from ~520 to 70 ka with

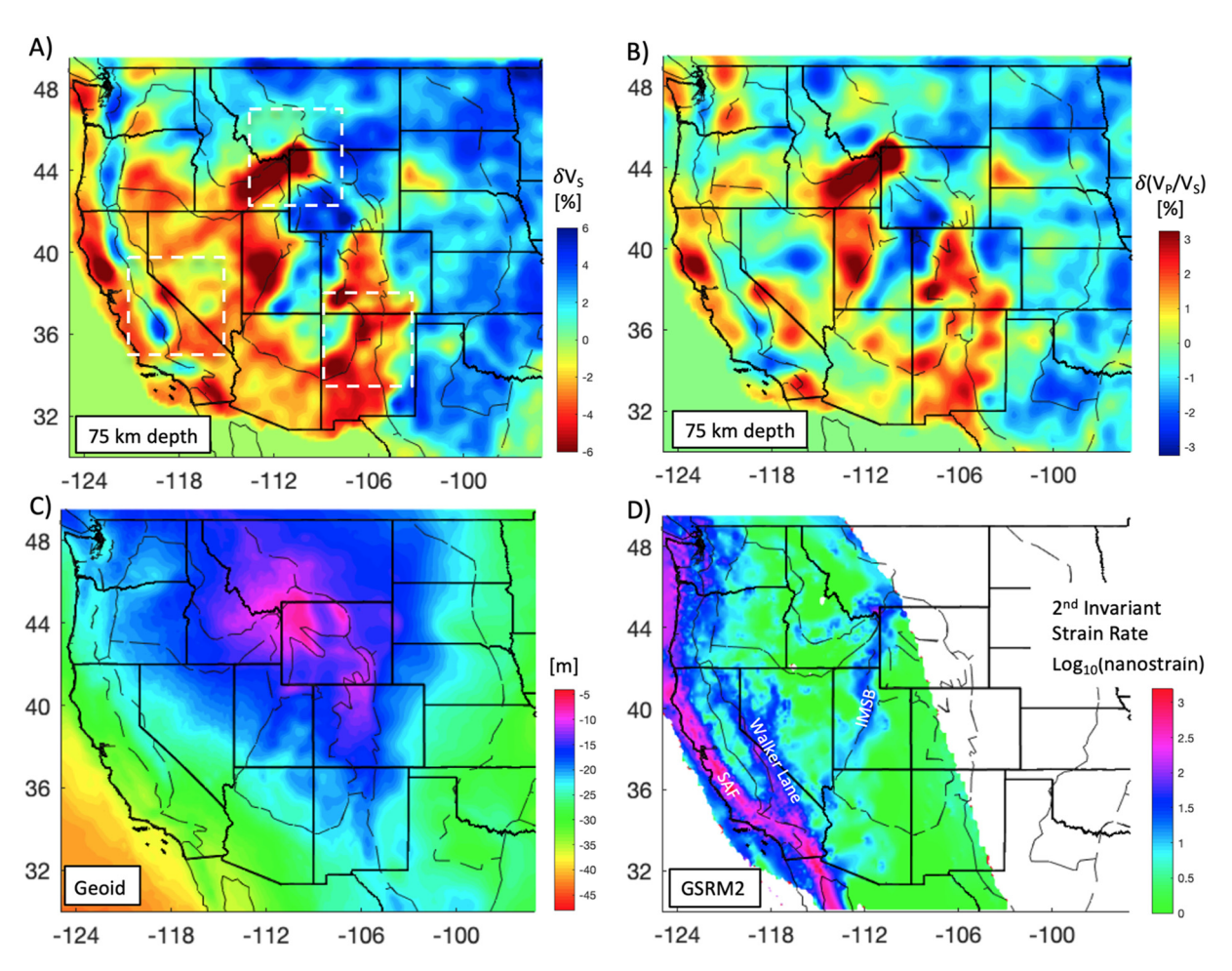


Fig. 2. Large-scale geophysical settings. A) Uppermost mantle tomography ~75 km dV_S (Schmandt and Lin, 2014) with inset boxes used in other figures labeled for each system. B) 75 km dV_P/V_S (Schmandt and Lin, 2014). C) Geoid surface (Smith and Milbert, 1999). D) Second invariant of horizontal strain rate from Global Strain Rate Map 2 constrained by GPS geodesy (Kreemer et al., 2014). The second invariant is a combined measure of shear and dilational strain rate in the horizontal plane. White areas are assumed to be rigid. Locations of the San Andreas Fault zone (SAF), Walker Lane, and Intermountain Seismic Belt (IMSB) are labeled on relatively high strain rate regions (Kreemer et al., 2014; Smith and Sbar, 1974; Herrmann et al., 2011).

typical volumes on the order of 10 km³ DRE, but including some as large as ~70 km³ DRE, and a cumulative volume > 600 km³ DRE (Christiansen et al., 2007; Watts et al., 2012). The youngest intracaldera rhyolitic lavas erupted ~70 ka (Christiansen, 2001). Modern indications of unrest include geodetic observations of spatially heterogeneous episodes of uplift and subsidence of the caldera at rates of up to 7 cm/yr and a spatial distribution consistent with volume changes at ~7–10 km depth (Chang et al., 2007, 2010). Dilational earthquake mechanisms and swarm seismicity further support fluid migration and/or degassing of a magmatic system at ~10 km depth (Taira et al., 2010; Farrell et al., 2010; Shelly et al., 2013).

2.2. Long Valley caldera

Long Valley caldera is located in the Walker Lane transtensional corridor at the eastern edge of the low-strain rate Sierra Nevada block (Fig. 2D), where intraplate dextral shear likely initiated in response to growth of the Pacific-North America transform margin and inheritance of thermally weakened lithosphere due to Ancestral Cascades arc magmatism (Atwater and Stock, 1998; Faulds et al., 2008; Busby, 2013). The caldera position coincides with a step-over in the eastern Sierra Nevada range-bounding fault system (Bailey et al., 1976). Geodetic studies show that transtensional deformation in the Walker Lane accommodates about one-fifth of Pacific North America relative motion (~10 mm/yr dextral motion) and this high strain rate corridor hosts a high concentration of modern geothermal resources (Bennett et al., 2003; Hammond and Thatcher, 2004; Faulds et al., 2012).

The area of Long Valley caldera became a rhyolitic volcanic center starting at ~2.2 Ma (Bailey et al., 1976; Metz and Mahood, 1991). The Bishop tuff-forming eruption of ~650 km³ DRE at 0.76 Ma (Andersen et al., 2017; Hildreth and Wilson, 2007) was followed by additional rhyolitic eruptions totaling ~100 km³ DRE between 0.76 and 0.65 Ma and ~400 m of resurgent dome uplift (Hildreth, 2004). Eruptions from the resurgent dome have not occurred since ~0.5 Ma and there is evidence of declining vigor of hydrothermal activity since ~0.3 Ma (Hildreth, 2017). These changes are consistent with the interpretation that the Bishop tuff-forming magmatic system is not in a state of active recharge (Hildreth, 2017), or that any active recharge is recent and deep enough that it has not yet influenced temperature measurements in the Long Valley Exploration Well (Flinders et al., 2018; Pribnow et al., 2003), Recent and ongoing recharge is favored by studies of modern geodetic unrest including uplift of the resurgent dome and microgravity measurements consistent with magma intrusion at depths of ~7-9 km (Battaglia et al., 1999; Tizzani et al., 2009; Montgomery-Brown et al., 2015). Total dome uplift since 1980 is ~0.8 m (Montgomery-Brown et al., 2015). Non-double-couple earthquakes consistent with volume increases at depth are observed beneath Long Valley caldera, but many occur at depths shallower than the geodetically inferred inflation source and may be interpreted as tensile crack opening events due to migration of CO₂ or other magmatic volatiles (Dreger et al., 2000; Foulger et al., 2004).

2.3. Valles caldera

Valles caldera is located at the intersection of the northeast-trending Jemez volcanic lineament and the north-trending Rio Grande Rift (Fig. 1; Heiken et al., 1990). With limited geochronological constraints, Suppe et al. (1975) noted that the volcanic lineament is approximately parallel to estimates of North America plate motion leading to its inclusion in some lists of hotspot tracks. However, subsequent advances in Jemez lineament geochronology do not support a hotspot-like spatiotemporal propagation of volcanism (e.g., Lipman and Mehnert, 1980). The orientation of the Jemez volcanic lineament is thought to be controlled by the Proterozoic lithospheric boundary between the Yavapai-Mazatzal Transition Zone and the Mazatzal province, which may provide favorable pathways for ascent of mantle melts leading to a

persistent weak zone in the lithosphere (Fig. 1D; Heiken et al., 1990; Karlstrom and Humphreys, 1998). Intersection of this zone of lithospheric weakness with Rio Grande Rift extension likely focuses magmatism at the location of Valles caldera. Extension began in the Rio Grande rift ~25 Ma (Ricketts et al., 2016; Landman and Flowers, 2013; Olsen et al., 1987). Starting at ~16 Ma compositionally diverse volcanism is recorded in the stratigraphy of the Jemez volcanic field encompassing Valles caldera, with dominantly mafic volcanism lower in the section and increasing rhyolitic deposits after ~7–8 Ma (Heiken et al., 1990; Goff et al., 2011).

Two VEI ≥ 7 Quaternary rhyolitic eruptions occurred in the area of Valles caldera (Heiken et al., 1990; Goff et al., 2011). The first was the lower (Otowi member) Bandelier tuff-forming rhyolitic eruption of ~380 km³ DRE at 1.62 Ma, which created Toledo caldera (Izett and Obradovich, 1994; Cook et al., 2016). The second was the upper (Tshirege member) Bandelier tuff-forming eruption of ~300 km³ DRE at 1.25 Ma, which created Valles caldera (Crosweller et al., 2012; Phillips et al., 2007). There were several smaller eruptions in the intervening ~0.4 Ma (Spell et al., 1996). Following the upper Bandelier tuffforming eruption resurgent dome uplift and rhyolitic volcanism occurred within ~30 ka including ~1 km of total resurgent uplift that was likely driven by recharge of the magma reservoir that produced the Bandelier tuff (Phillips et al., 2007; Kennedy et al., 2012). The youngest rhyolitic lavas in Valles caldera based on structural relationships proved difficult to accurately date for many years (e.g., Wolff and Gardner, 1995; Reneau et al., 1996; Zimmerer et al., 2016). The most recent geochronology indicates that the youngest eruptions occurred ~68–74 ka at the conclusion of a protracted period of magmatism during the preceding ~350 ka (Zimmerer et al., 2016). Unlike Yellowstone and Long Valley calderas, there is no evidence of modern unrest in the form of geodetically constrained vertical deformation and there is a paucity of local seismicity (House and Hartse, 1995; Nakai et al., 2017). However, another contrast with Yellowstone and Long Valley is that there are not continuous and publicly accessible GPS or microearthquake monitoring networks in Valles caldera, so there is more limited potential for the geophysics research community to detect potential subsurface unrest. Regional scale horizontal deformation surrounding the Rio grande Rift is constrained by GPS geodesy, which finds slow but significant strain rates with recent estimates of ~0.1 mm/yr of extension across 100-km West-East transects of the Rio Grande rift (Fig. 2D; Berglund et al., 2012; Kreemer et al., 2014). It should be noted that horizontal strain rates near Valles caldera are ~2 orders of magnitude slower than in the areas surrounding Long Valley and Yellowstone calderas (Fig. 2D; Kreemer et al., 2014).

3. Methods for seismic imaging of crustal and upper mantle magmatic systems

This review largely focuses on natural (passive) source seismic methods that enable crustal and/or uppermost mantle scale imaging because it is an area of substantial progress in the past two decades. The purpose of this section is to give a brief introduction to natural source methods that have been heavily used, and in some cases developed, in recent years. It is not an exhaustive survey of methods because it prioritizes techniques relevant to the following discussion of structures beneath Yellowstone, Long Valley, and Valles calderas.

3.1. Body wave tomography

Teleseismic or local body wave tomography inversions are most commonly conducted using travel time measurements to infer 3D variations in P and/or S velocity structure (Lees, 2007). Teleseismic ray path coverage generally provides angles of incidence between ~10–40° and azimuthal coverage depends on the distribution of distant plate boundaries and areas of frequent intraplate seismicity with respect to the study area. In the western U.S., teleseismic data coverage is favorable

from the southeast, southwest, and northwest directions, but teleseismic earthquakes from the northeast are relatively scarce due to lower seismicity rates in the North Atlantic and Arctic oceans, Local earthquake tomography provides path coverage that may include angles of incidence from 0 to 90° (due to turning paths within the crust) and highly variable azimuthal coverage depending on the distribution of local earthquakes and seismographs. One significant challenge of local earthquake tomography is that for local volcano monitoring networks there is often little sensitivity to structure at depths below most local earthquake hypocenters (e.g., Seccia et al., 2011; Lin, 2015; Farrell et al., 2014). Seismicity in the volcanic settings of interest primarily occurs at depths less than ~6–8 km such that most local ray paths overlie or only partially sample crustal magma reservoirs. Limitations due to the depth distribution of local seismicity can be mitigated through joint inversion of local and teleseismic body wave travel times (Huang et al., 2015). However, steeply incident teleseismic ray paths (rather than rays that turn within the crust) only constrain relative and not absolute velocity variations. Another challenge common to both teleseismic and local earthquake tomography studies is that the first-arriving seismic energy is deflected around strong lowvelocity anomalies. The effects of ray bending around low-velocity anomalies can be mitigated through use of 3D ray tracing or wave front tracking algorithms (Weiland et al., 1995) and eventually by application of full waveform tomography to high-frequency body wave measurements (e.g., Yuan et al., 2015). Full waveform tomography refers to methods that compute the full 3D wave field for the forward problem and iteratively calculate 3D sensitivity kernels that relate the misfit of waveform measurements (e.g., frequency-dependent travel times and/or amplitudes) to changes in 3D structural models. Full waveform tomography studies of magmatic systems to date have focused on surface wave measurements (Liu et al., 2017; Flinders and Shen, 2017; Flinders et al., 2018), but it is reasonable to expect applications to magmatic systems to broaden to include body waves and higher frequencies as computational workflows, computing power, and seismic data sets continue to improve (Krischer et al., 2015).

3.2. Surface wave tomography

Most modern surface wave tomography studies of magmatic systems do not rely on earthquakes or controlled sources, instead they rely on ambient noise interferometry to obtain estimates of interstation Green's functions (Shapiro and Campillo, 2004; Sabra et al., 2005). This enables seismographs to serve as virtual sources and it gives seismologists greater control over the design of source-receiver paths than in natural source surveys (e.g., Lin et al., 2009). Given that the Green's function estimates are for surface sources, surface waves are generally the largest amplitude features (Shapiro and Campillo, 2004; Sabra et al., 2005). Interferometry with vertical channel data is used to extract Rayleigh wave signals that are dominantly sensitive to vertically polarized shear wave velocity (V_{SV}), and the transverse component is used to extract Love wave signals sensitive to horizontally polarized shear wave velocities (V_{SH}; e.g., Lin et al., 2008). Inter-station measurements of surface wave dispersion are the most commonly exploited information in surface wave tomography. The ability to recover short-period surface waves with noise interferometry has greatly expanded the use of surface wave imaging in volcanic settings since Brenguier et al. (2007).

Conventionally, most surface wave tomography is conducted in two steps (Fig. 3B). First, an ensemble of phase or group velocity maps are constructed by performing a 2D tomography inversion of inter-station velocity measurements at different periods (e.g., Barmin et al., 2001). Second, the set of phase and/or group velocities at each geographic location (dispersion curves) are used to invert for V_S as a function of depth and the locally 1D V_S models are combined to form a 3D V_S model (e.g., Masterlark et al., 2010; Shen and Ritzwoller, 2016). Depth resolution is enabled by the different

sensitivity kernels of each period measured, but there is considerable overlap in the sensitivities such that each period is not strictly an independent measure of subsurface structure (Fig. 3B). In this conventional approach the effects of topography are ignored, but topography can alter surface wave dispersion and cause transfer of energy to scattered phases (e.g., Gilbert and Knopoff, 1960; Snieder, 1986; Borisov et al., 2017; Ping et al., 2018). Surface wave inversion methods that incorporate 2D and 3D topography are becoming more computationally feasible, but their use is not yet widespread in studies of volcanic systems (Borisov et al., 2017; Li et al., 2019). Full waveform tomography uses numerical modeling of the entire 3D wave field, or part of it during time windows of interest, to compute sensitivity kernels specific to the waveforms for each source-receiver pair rather than those based on 1D reference models (Fig. 3C; e.g., Tape et al., 2010; Lee et al., 2014). Full waveform inversions in 3D are computationally expensive but provide a natural way to simultaneously model multiple waves types and use more realistic parameterizations that include topography (e.g., Yuan et al., 2015; Borisov et al., 2017). Recent applications in volcanic settings still use surface wave phase measurements as their input data (Flinders and Shen, 2017; Liu et al., 2017; Flinders et al., 2018), so there remains potential for improvement where it is possible to incorporate additional data including 3-component amplitudes for surface waves, higher frequency P and S body waves, and later-arriving scattered surface or body waves.

3.3. Natural source scattered wave imaging

The majority of the imaging constraints reviewed here are from tomographic inversions for smooth seismic velocity variations, but important complementary constraints on the magmatic systems are afforded by imaging of interfaces that mark abrupt changes in seismic properties and give rise to scattered wave phases. Forward scattering refers to seismic phases that are transmitted through the interface and the most often exploited forward-scattered phases are teleseismic P-to-S conversions (e.g., Steck and Prothero, 1994; Chu et al., 2010; Seccia et al., 2011), which result from transferring a fraction of seismic wave energy between compressional and shear waves at the interface (Fig. 3D). Many converted wave imaging studies assume locally horizontal interfaces (e.g., Seccia et al., 2011), but if high density seismic arrays are available then more accurate migration approaches can potentially constrain 2D or 3D structures with dipping, curved, or truncated interfaces (Bostock and Rondenay, 1999; Poppeliers and Pavlis, 2003; Liu and Levander, 2012; Shang et al., 2012; Hansen and Schmandt, 2017). More commonly in volcanic fields, only a small number of seismographs sample interfaces of interest and 3D migration is not feasible. In that case, forward modeling of the teleseismic scattered waves in 2D or 3D with wave field simulations or ray tracing can provide valuable but spatially isolated constraints on dipping or discontinuous interfaces (e.g., Chu et al., 2010; Steck and Prothero, 1994; Schlue et al., 1996). Other 3D scattered wave imaging approaches use coda from local earthquakes, eruptions, or surface processes to image smooth variations in scattering intensity but do not necessarily locate distinct interfaces (Tramelli et al., 2006; De Siena et al., 2014; Prudencio et al., 2018; Chaput et al., 2012; Zandomeneghi et al., 2013).

Other scattered wave analyses rely on back-scattered phases that are reflected by sharp interfaces. Free-surface multiples of teleseismic waves reflect off the free-surface boundary and then reflect again at subsurface interfaces allowing reflection images to be made without local sources such as earthquakes or controlled sources (Fig. 3E; e.g., Aprea et al., 2002). This approach has the practical advantage of its compatibility with migration algorithms that were initially developed for reflection imaging with local controlled sources at the surface such as explosions or vibrator trucks. If local seismicity occurs within sufficiently dense seismograph networks then it is possible to use

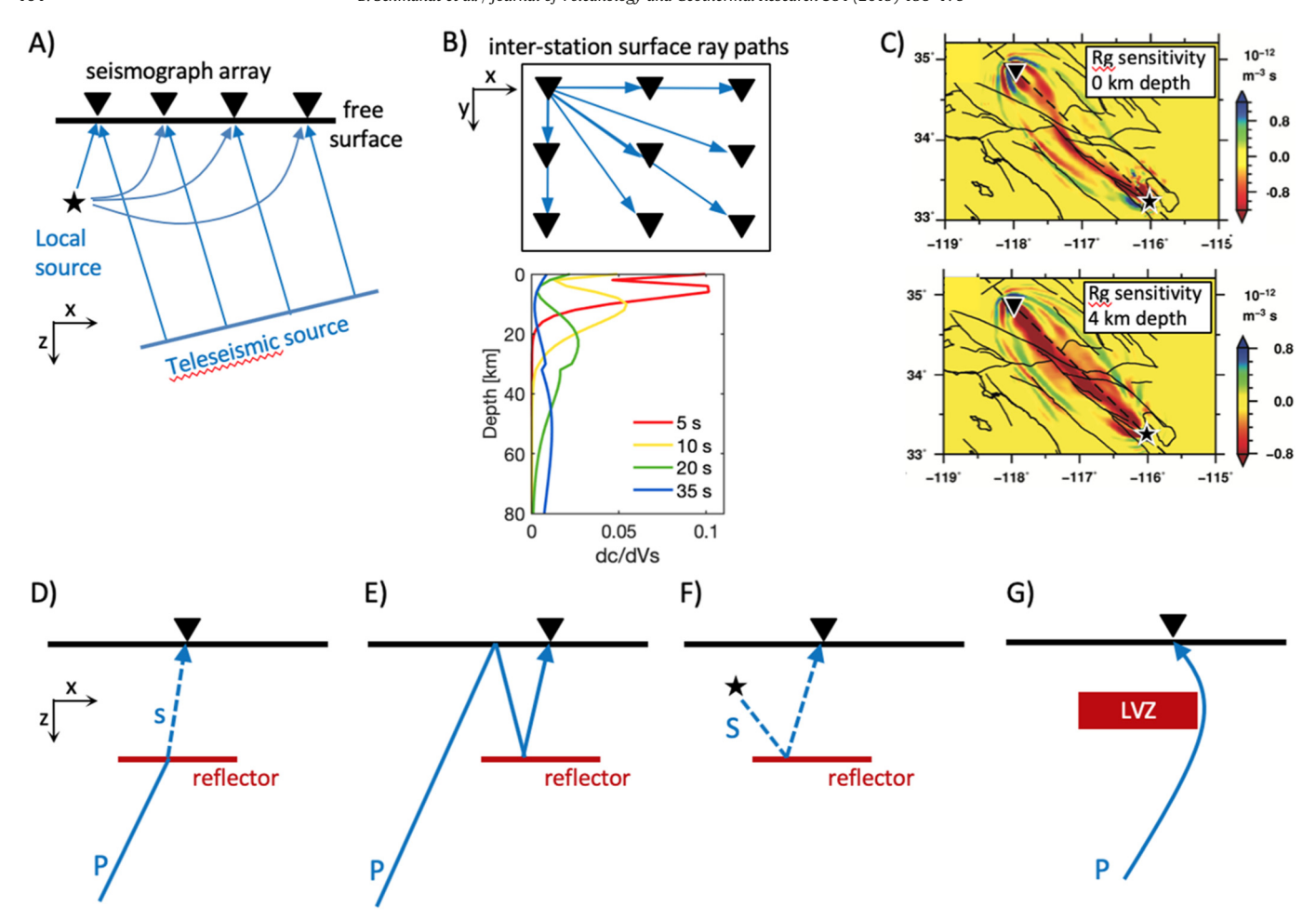


Fig. 3. Graphical representations of different types of seismic sampling of the subsurface. A) Local & teleseismic body wave ray path travel time tomography. B) Two-step surface wave dispersion tomography using inter-station velocities to create phase or group velocity maps and then inverting dispersion curves at each point for 1D Vs structure. Note that Rayleigh wave depth sensitivity kernels are plotted but the detailed shape depends on the reference model and the shapes of Love wave kernels would be different. C) A full wave numerical sensitivity kernel for a cross-correlation measurement of the travel time of the first-arriving Rayleigh (Rg) wave (filtered from 3 to 30 s period) for a specific earthquake source and seismic receiver pair in southern California (modified from Tape et al., 2010). The kernel is plotted at depths of 0 and 4 km. The star represents the earthquake source and the triangle represents the receiver. Thin black lines show faults and the coast. D) Steeply incident teleseismic P waves have approximately planar wave fronts and when they encounter seismically reflective interfaces they convert a fraction of their wave energy to a S wave often referred to as Ps to denote the P-to-S conversion. E) Another way to use scattering of teleseismic P waves for receiver-side imaging is to apply processing to isolate reflections from the free-surface reflected P wave and migrate the signals to form a reflection image. F) Local earthquakes are effective as sources for reflections from underlying magmatic systems and partial melt can cause particularly strong S-wave reflections. G) Anomalous arrival angles of teleseismic waves can identify extreme low-velocity zones (LVZ). In the example the teleseismic P wave would approach the receiver from the left side in the absence of the LVZ, but it approaches from the right side because it is deflected by the LVZ.

reflected arrivals to map the locations and properties of potential magmatic interfaces (e.g., Sanders, 1984; Zucca et al., 1987; Nakata and Shelly, 2018). A recent example takes advantage of swarm seismicity, which is relatively common in volcanic settings, to isolate reflections from the roof of an inferred magma reservoir (Nakata and Shelly, 2018).

4. Seismic imaging constraints

This section takes a bottom-up perspective by sequentially considering seismic constraints on magmatic system structure from the upper mantle to the upper crust. Many studies inform the modern state of knowledge about each magmatic system. The example images included in the figures prioritize seismic results that are based on up-to-date data resources and provide constraints on vertically integrated magmatic system structure throughout the crust and in some cases the upper mantle. This approach is meant to facilitate subsequent synthesis of the seismic results in the context of multidisciplinary constraints on the three large silicic magmatic systems in Section 5.

4.1. Upper mantle melt

At upper mantle depths from the Moho to ~100 km excellent opportunities for inter-regional comparison come from many recent studies that exploited EarthScope's TA data set along with varying amounts of local monitoring and past temporary array data (e.g., Burdick et al., 2010; Schmandt and Humphreys, 2010; Obrebski et al., 2011; Wagner et al., 2010; Gilbert et al., 2012; Shen and Ritzwoller, 2016). Near the three calderas of interest, the presence of low seismic velocity anomalies in the upper mantle was previously constrained by regional or local scale studies (e.g., Waite et al., 2006; Schutt and Dueker, 2008; Yang and Forsyth, 2006; West et al., 2004; Slack et al., 1996; Humphreys and Dueker, 1994). However, wide-aperture arrays such as the TA are valuable for extending and/or improving resolution in the upper mantle where imaging may not be possible with local monitoring arrays alone. Also, by seamlessly connecting smaller isolated arrays across the western U.S., the TA data provide improved opportunities for inter-regional comparison of tomography models with a common minimum level of sampling.

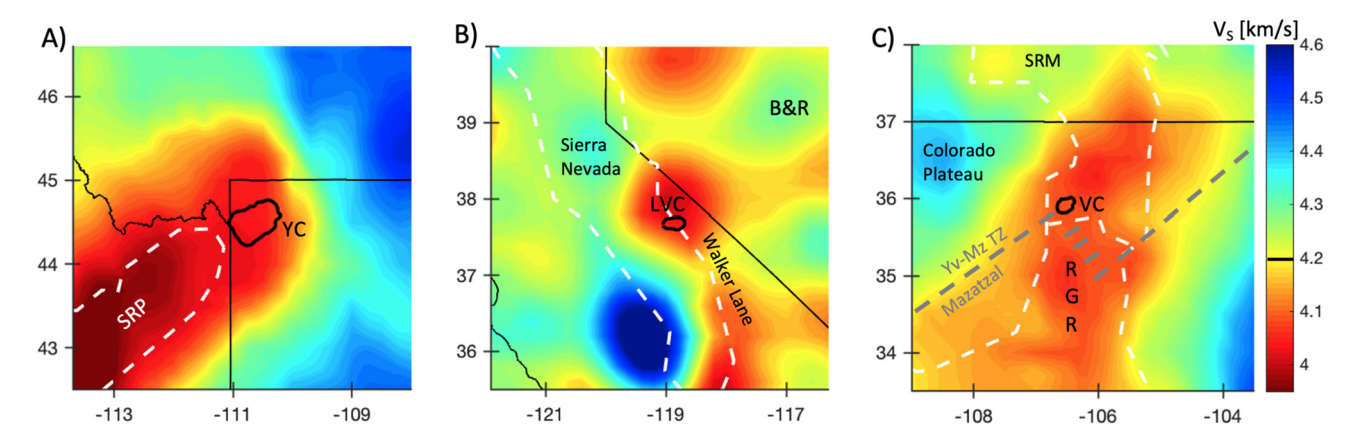


Fig. 4. Regional V_S tomography maps at 75 km depth. A) Rayleigh wave V_S tomography model from Shen and Ritzwoller (2016) with the Snake River Plain (SRP) and Yellowstone caldera (YC) labeled. B) Joint Rayleigh and S-wave V_S tomography model from Jiang et al. (2018b) with the Sierra Nevada, Walker Lane, Basin and Range (B&R), and Long Valley caldera (LVC) labeled. C) Rayleigh wave V_S tomography model from Shen and Ritzwoller (2016) with the Colorado Plateau, southern Rocky Mountains (SRM), Rio Grande Rift (RGR), Yavapai-Mazatzal transition zone (Yv-Mz TZ), Mazatzal province (Mz), and Valles caldera (VC) labeled. Areas with $V_S < 4.2$ km/s at 75 km depth are considered likely to host partial melt and this threshold is marked on the color scale.

Fig. 4 shows Vs inversion results for the upper mantle from studies that used TA data and regional networks (Shen and Ritzwoller, 2016; Jiang et al., 2018b). As noted in the preceding paragraph there are many other relevant imaging studies. The models shown in Fig. 4 were chosen as examples because they reflect the state of knowledge following the TA deployment and they use multiple types of seismic information to constrain upper mantle Vs. The U.S. scale model from Shen and Ritzwoller (2016) inverted measurements of Rayleigh wave dispersion and station-averaged receiver functions, and it is shown for the regions near Yellowstone and Valles calderas. The southwestern U.S. model of Jiang et al. (2018b) inverted measurements of surface wave dispersion and teleseismic S-wave travel time residuals. This model was chosen for the region near Long Valley because it includes data from the Sierra Nevada EarthScope Project (Frassetto et al., 2011; Gilbert et al., 2012), which provides enhanced resolution of upper mantle Vs structure beneath Long Valley caldera compared to models only using the TA data. The low-Vs anomaly near the Yellowstone hotspot is large enough to be well resolved by any model using the TA data, and there is not an upper mantle Vs model that couples TA data with denser array data covering Valles caldera.

Upper mantle seismic velocities depend on many factors including temperature, bulk composition, grain size, oxidation state, and partial melt fraction (e.g., Schutt and Lesher, 2006; Afonso et al., 2010; Jackson and Faul, 2010; Cline II et al., 2018; Hammond and Humphreys, 2000; Schmeling, 1985; Takei, 2017). Consequently, melt fraction estimates based on seismic velocities (V_P and/or V_S) are generally non-unique, but it is often possible to make useful inferences in cases where seismic velocities strongly deviate from global mean values or physical model predictions for reference geotherms and compositions (e.g., Dalton and Faul, 2010). It is difficult to explain V_S ≤ 4.2 km/s in the shallow upper mantle, ~75 km depth, with subsolidus temperatures, but further reductions in V_S are readily explained by the addition of small partial melt fractions (Takei, 2017; Faul and Jackson, 2005; Plank and Forsyth, 2016). A study of isostatic support for Cordilleran topography suggests that V_S reductions below a higher threshold of ~4.37 km/s may be best explained by partial melt to avoid unrealistic estimates of thermal buoyancy (Levandowski et al., 2014); although, nonlinear changes in elastic moduli at temperatures just below the solidus offer an alternative interpretation for V_S between ~4.37-4.2 km/s at 75 km depth (Takei, 2017). Melt fraction estimates also exhibit uncertainty because there are a variety of scaling predictions ranging from ~3-8% V_S reduction per percent of melt in the upper mantle (at nearsolidus conditions), with much of the variability owing to the effects of different assumed wetting angles for intergranular melts (e.g., Schmeling, 1985; Hammond and Humphreys, 2000; Takei, 2002). V_S tomography maps surrounding each caldera show that they are all underlain by shallow upper mantle with $V_S < 4.2$ km/s (Fig. 4). The low- V_S areas also exhibit relatively high V_P/V_S , as expected for partial melt (Schmeling, 1986; Hammond and Humphreys, 2000; Takei, 2002), and they are concentrated beneath Quaternary volcanic fields of the western U.S. (Fig. 1A & 2B; Schmandt and Humphreys, 2010).

Yellowstone caldera sits at the northeastern edge of exceptionally low-velocity upper mantle beneath the eastern Snake River Plain, Long Valley caldera overlies a concentrated low-velocity anomaly within the Walker Lane, and Valles caldera is located above broad low-velocity trends associated with the Rio Grande Rift and the Jemez volcanic lineament (Figs. 2 & 4). Beneath the easternmost Snake River Plain and beneath Long Valley caldera upper mantle V_S at 75 km depth reaches ~3.8-4.05 km/s (Schutt et al., 2008; Shen and Ritzwoller, 2016; Jiang et al., 2018b). These velocities are similar to or up to ~0.2 km/s lower than those found beneath the East Pacific Rise where rapid production of oceanic crust requires a steady flux of melt from the upper mantle (Schutt and Dueker, 2008; Harmon et al., 2009; Forsyth and Scheirer, 1998). If V_S reduction below 4.2 km/s in the tomography shown in Fig. 4 is attributed to partial melt, it implies: ~0.5-1.5% beneath Yellowstone caldera, ~1-3% beneath the Snake River Plain, ~0.7–2% beneath Long Valley caldera, and ≤1% beneath Valles caldera. Two values are included for the Yellowstone region because propagation of the hotspot into the Wyoming craton juxtaposes supersolidus upwelling against cold mantle lithosphere and those effects may be averaged in the travel time or dispersion measurements.

4.2. Lower crustal magma reservoirs

Relative to upper mantle imaging largely enabled by the TA, denser composite arrays (combining stations from different time periods) around calderas are often needed to enable imaging local-scale lower crustal structures. Body wave tomography imaging of the lower crust beneath the calderas typically requires use of teleseismic data (e.g., Weiland et al., 1995; Steck et al., 1998; Huang et al., 2015). Surface wave dispersion measurements spanning periods of ~15-35 s also constrain lower crustal structure (e.g., Stachnik et al., 2008; Flinders et al., 2018; Jiang et al., 2018a). The example images in Figs. 5-7 were chosen because they provide coherent views of the transcrustal magmatic systems using up-to-date data resources. Fig. 5 shows images of the region near Yellowstone caldera including a P-wave travel time tomography inversion that used local and teleseismic data (Fig. 5A; Huang et al., 2015) and surface wave tomography inversion that used Rayleigh and Love wave dispersion (Fig. 5B; Jiang et al., 2018a). Both

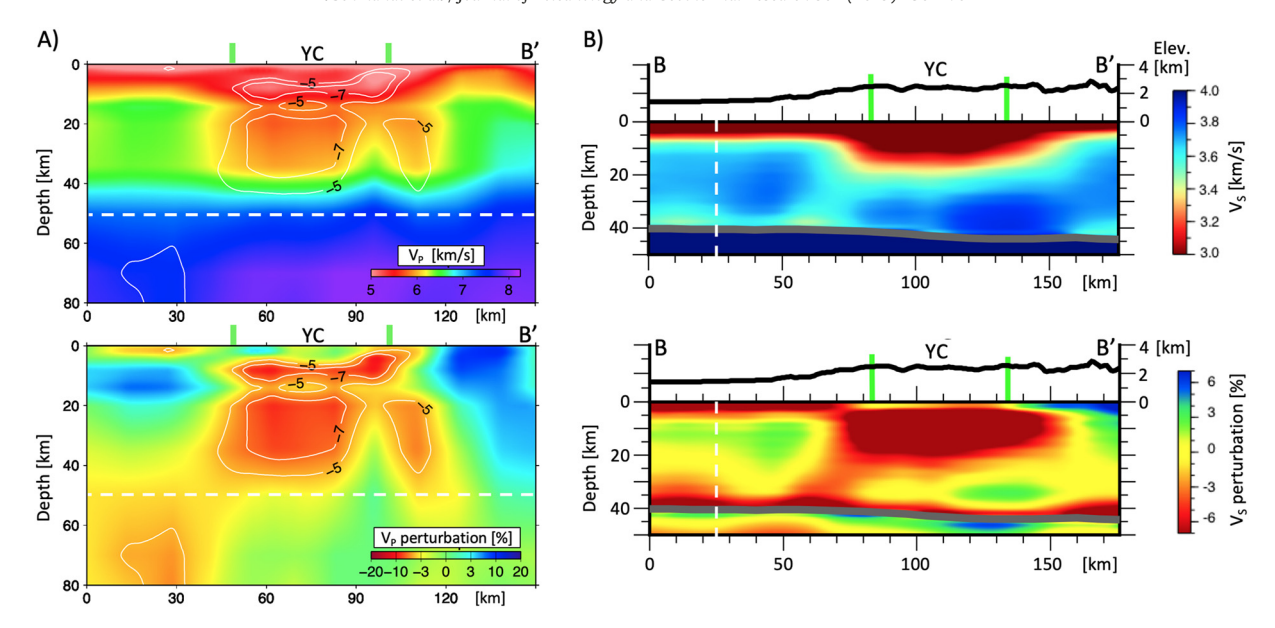


Fig. 5. Yellowstone crust and uppermost mantle tomography. A) The location of the cross-section is shown in Fig. 1C. Absolute and relative V_P travel time tomography images are shown in the top and bottom panels, respectively (modified from Huang et al., 2015). Absolute V_P is not well constrained below ~20 km due to lack of local earthquake ray paths. The absolute V_P from the starting model controls the position of ray paths in the inversion and V_P perturbations at depths >20 km are dominantly constrained by teleseismic travel time residuals. The horizontal white dashed lines mark the maximum depth of the V_S tomography images shown in (B). Yellowstone caldera (YC) boundaries are denoted by green vertical lines. B) Absolute and relative isotropic V_S tomography images from surface waves are shown in the top and bottom panels, respectively (modified from Jiang et al., 2018a). The cross-section used by Jiang et al. (2018a) starts 25 km farther southwest beneath the Snake River Plain and the vertical white dashed line shows the southwestern limit of the cross-sections from Huang et al. (2015) shown in (A). Yellowstone caldera (YC) boundaries are denoted by green vertical lines.

studies combined TA data with denser regional network data. Fig. 6 shows one V_P tomography model and two V_S tomography models for the region near Long Valley caldera. The V_P model was chosen because it uses a through set of travel times from local-to-regional earthquakes and controlled sources to provide resolution through the crust (Fig. 6A; Lin et al., 2010). One V_S model used a locally 1D method to invert Rayleigh and Love wave dispersion measurements (Fig. 6B; Jiang et al., 2018a) and the other used a 3D full waveform tomography method to invert measurements of Rayleigh wave dispersion (Fig. 6C; Flinders et al., 2018). Two V_S were chosen because they both provide sampling throughout the crust and viewing the isotropic Vs inversion results from Jiang et al. (2018a) provides relevant context for discussion of that model's anisotropic structure in Section 4.4.

Seismic tomography provides potential evidence of lower crustal magma reservoirs beneath each of the three calderas (Huang et al., 2015; Jiang et al., 2018a; Dawson et al., 1990; Weiland et al., 1995; Lin et al., 2010; Steck et al., 1998; Aprea et al., 2002). However, the potential lower crustal reservoirs exhibit subtler velocity reductions compared to the middle-to-upper crustal reservoirs discussed in the next section (Weiland et al., 1995; Steck et al., 1998; Huang et al., 2015; Jiang et al., 2018a). Additionally, the detailed location and geometry of potential lower crustal reservoirs exhibits greater variability between body and surface wave tomography than the middle-to-upper crustal depths in the magmatic systems.

Beneath Yellowstone caldera joint local and teleseismic P-wave travel time tomography identified a low V_P anomaly at depths of ~20–40 km that is distinct from the middle-to-upper crustal reservoir previously imaged using only local earthquake data (Fig. 5A; Huang et al., 2015; Farrell et al., 2014). The inferred lower crustal reservoir's V_P is ~6.5% lower than the regional mean, which was interpreted to represent ~2% mafic melt across a total reservoir volume of ~46,000 km³, which corresponds to ~900 km³ mafic magma (Huang et al., 2015). A subsequent surface wave tomography model of the Yellowstone region also finds a lower crustal V_S anomaly; however, its position partially overlaps the southwestern portion of the V_P anomaly and extends farther beneath Snake River Plain (Fig. 5; Jiang et al., 2018a). Somewhat

different lower crustal imaging results are also found beneath Long Valley caldera (Fig. 6). Teleseismic P wave travel time tomography resolved a low- V_P anomaly of ~10–15% from ~20–30 km depth (Weiland et al., 1995). However, P wave tomography using an extensive compilation of travel times from local-to-regional earthquakes and controlled sources finds weaker, ~5-10%, low-Vp anomalies in the lower crust west and east of Long Valley caldera, but not directly beneath it (Lin et al., 2010). Full waveform V_S tomography applied to Rayleigh wave dispersion measurements up to 30 s period at Long Valley also did not identify a distinct lower crustal low-velocity anomaly beneath the caldera (Fig. 6C; Flinders et al., 2018). A different Rayleigh and Love wave tomography study using a local 1D inversion approach found a weak lower crustal low-V_S anomaly that dips to the west (Fig. 6B; Jiang et al., 2018a), where it overlaps deep crustal seismicity and more localized magmatic structures inferred beneath Mammoth Mountain (Hotovec-Ellis et al., 2018; Shelly and Hill, 2011). Interpretation of the potential lower crustal reservoir is complicated by the fact that largerscale surface tomography inversions suggest that the V_S anomaly just west of Long Valley caldera extends along the strike of the Sierra Nevada south of Long Valley (Jiang et al., 2018b), so its specific connection to rhyolitic magmatism at Long Valley is unclear. At Valles caldera, only body wave tomography models are available with a level of resolution that might reveal a deep crustal magma reservoir. Teleseismic P wave tomography beneath Valles caldera shows ~10–15% low-V_P anomalies in the lower crust between ~30-40 km depth (Steck et al., 1998) and these features are co-located with abrupt interfaces detected by migration of back-scattered teleseismic P waves (Fig. 7; Aprea et al., 2002). The interfaces may represent layering of partially molten and fully crystallized sills in the lower crust (Aprea et al., 2002).

4.3. Middle-to-upper crustal reservoirs

The strongest seismic evidence for magma reservoirs beneath the three calderas is found at middle-to-upper crustal depths (\sim 5–15 km). Seismic tomography inversions resolve smooth low-velocity anomalies of up to \sim 35% Vp and \sim 20% Vs relative to the surrounding regional crust (Weiland et al., 1995; Flinders et al., 2018; Huang et al., 2015; Steck

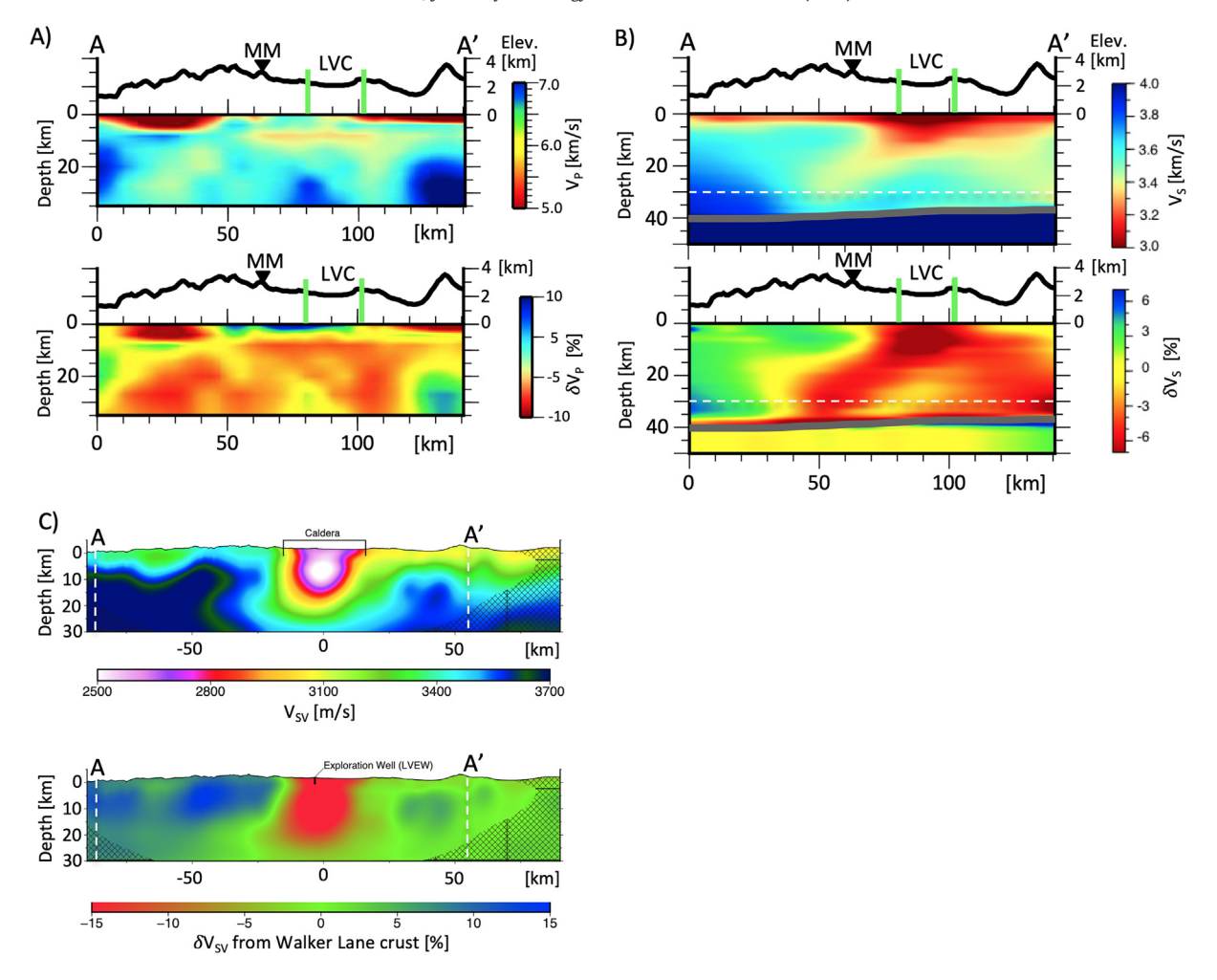


Fig. 6. Long Valley crustal tomography. A) The location of the cross-section is shown in Fig. 1B. Absolute (upper) and relative (lower) isotropic V_P travel time tomography results from Lin et al. (2010). The locations of Long Valley caldera (LVC) and Mammoth Mountain (MM) are labeled. B) Absolute (upper) and relative (lower) isotropic V_S tomography images from Rayleigh and Love wave tomography modified from Jiang et al. (2018a). The horizontal white dashed line bounds the maximum depth shown for the model in (C). C) Absolute (upper) and relative (lower) V_{SV} tomography images from full waveform inversion of Rayleigh wave dispersion modified from Flinders et al. (2018). The cross-section has the same strike as A-A' shown in Fig. 1B but the cross-section in panel C extends farther East and West. The cross-hatched areas near the ends are not well resolved. The vertical white lines bound the extent of the A-A' cross-section shown in (B). Long Valley caldera is labeled on the upper panel and the Long Valley Exploration Well is labeled on the lower panel.

et al., 1998), and scattered wave studies indicate that some smooth velocity anomalies identified by tomography actually have sharp upper, lower, and/or lateral edges consistent with higher melt fractions of ~30–60% (Chu et al., 2010; Seccia et al., 2011; Nakata and Shelly, 2018; Aprea et al., 2002). Tomography studies using only local earthquake data recorded by small-aperture arrays surrounding the calderas provide detailed resolution of the upper crust, but these models are better suited to analysis of the connections between the tops of the magma reservoirs and shallower hydrothermal systems, pyroclastic deposits, and faulting (e.g., Lin, 2015; Foulger et al., 2003; Seccia et al., 2011; Husen et al., 2004). Here, we focus on seismic imaging results that entirely sample transcrustal magmatic systems.

The seismically inferred middle-to-upper crustal reservoirs are notable for their large velocity anomalies and their mostly overlapping depth intervals beneath each of the three calderas. The middle-to-upper crustal reservoirs extend from ~5–16 km depth beneath Yellowstone caldera (Fig. 5; Huang et al., 2015), ~5–20 km depth beneath Long Valley caldera (Fig. 6; Flinders et al., 2018; Jiang et al., 2018a; Thurber et al., 2009; Lin et al., 2010), and ~5–16 km depth beneath Valles caldera (Fig. 7; Steck et al., 1998). Scattered wave studies of sharp interfaces indicate narrower depth intervals for the reservoirs or at least stratification with a layer of exceptionally low velocities in the upper portion of the tomographically inferred reservoirs (Fig. 8). At Yellowstone,

2-D forward modeling of teleseismic Ps conversions suggests a reservoir with a spatially heterogeneous thickness of ~3.6-5 km that is located deeper in the southeast and shallower in the northwest (Fig. 8A; Chu et al., 2010). The sharp edges of the reservoir create 'wrap-around' phases that arrive with the opposite polarity due to ray path bending to avoid the low-velocity magma reservoir. These phases are consistent with V_S reductions of ~66% (Chu et al., 2010). At Long Valley caldera inversion of teleseismic Ps conversions for locally 1-D velocity structure suggests V_S reductions of \sim 40% in a \sim 2–4 km thick layer with a top at \sim 7–9 km depth (Fig. 8B; Seccia et al., 2011). Both seismographs used for the receiver functions are located near the edge of the 3D magma reservoir so the assumption of 1D wave propagation for the receiver function inversion could be problematic. However, reflections from controlled source surveys and local earthquake swarms further support the presence of a ~8 km deep sharp top to the magma reservoir beneath Long Valley caldera (Hill et al., 1985; Nakata and Shelly, 2018). Additionally, localization of the lowest velocities near the top of the reservoir is consistent with local earthquake P wave travel time tomography (Seccia et al., 2011; Lin et al., 2010). At Valles caldera, teleseismic P wave migration imaging detects a sharp bottom to the magma reservoir (Fig. 7C; Aprea et al., 2002). The top of the magma reservoir beneath Valles caldera is not clearly resolved, possibly due to interference with a strong reflection from

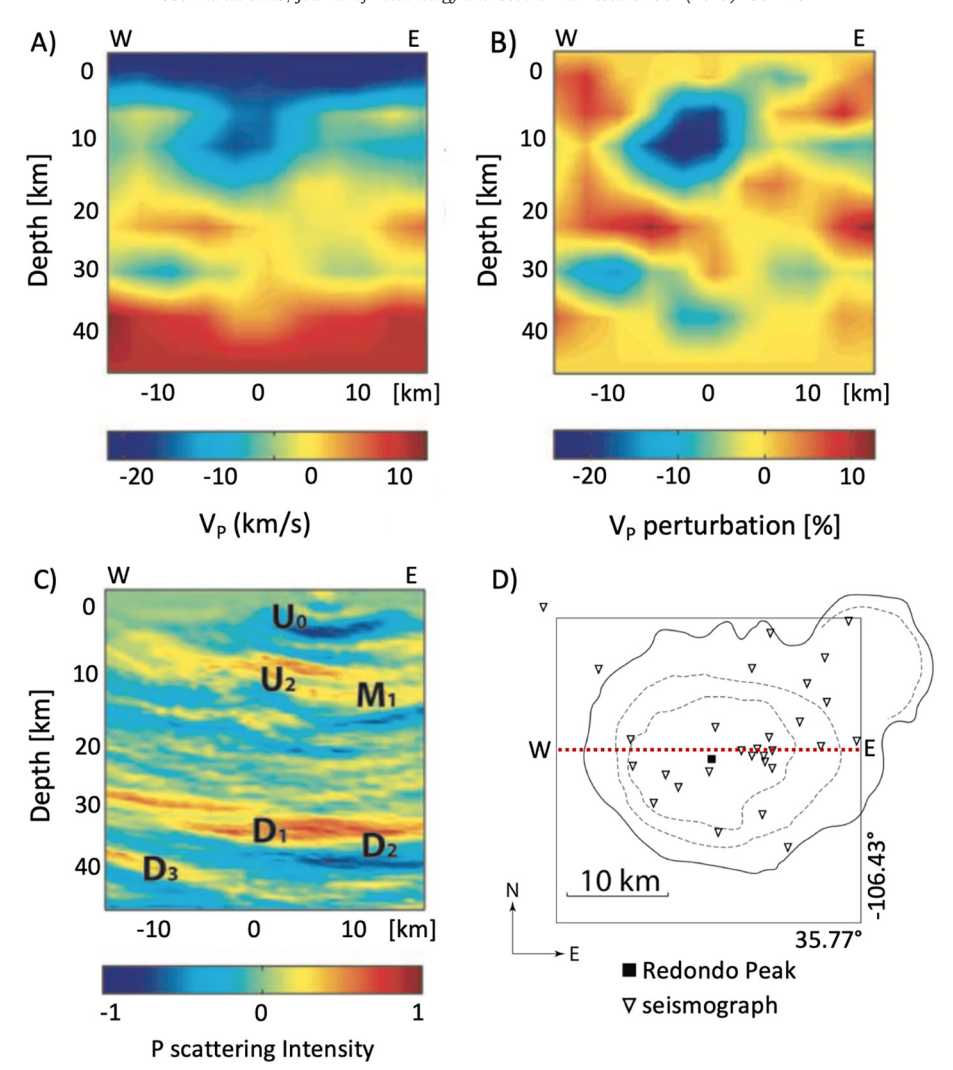


Fig. 7. Valles caldera tomography and scattered wave imaging. All figure panels are modified from Aprea et al. (2002). A) Absolute V_P teleseismic travel time tomography cross-section. Note that high velocities are shown in red and low velocities are shown in blue. The location of the cross-section is shown in (D). Absolute velocities are used for ray tracing but they are not well constrained by teleseismic travel time residuals. B) Same tomography cross-section as in (A) but the perturbations from the average 1D model are plotted. C) A cross-section through a scattered wave imaging volume made using scattered P arrivals in teleseismic P wave coda, modified from Aprea et al., (2002). The colors represent P wave reflectivity on a normalized scale, with positive values indicating velocity increasing with depth and negative values indicating velocity decreasing with depth. Upper crustal interfaces are thought to represent the base of caldera fill (U_0) and base of the magma reservoir (U_2). Middle (W_1) and lower crustal interfaces (D_{1-3}) are thought to represent a mix of partially molten or crystallized sills (Aprea et al., 2002). D) The map shows the JTEX stations used for the P wave migration imaging with the caldera rim contour in solid black and ring faults in dashed black. The black square shows the imaging domain for the P wave migration results shown in C and the dashed rel line shows the location of the cross-section shown in A-C. Some additional stations contributed travel time data for the tomography study (see Steck et al., 1998).

the base of the caldera or a complex geometry of the reservoir's roof (Aprea et al., 2002).

The average melt fractions and total volumes of the seismically inferred reservoirs provide some insight into the feasibility of future large eruptions. The total volume of the middle-to-upper crustal reservoir beneath Yellowstone caldera is the largest, ~10,000 km³ (Huang et al., 2015). Its estimated average melt fraction of ~9% corresponds to a total of ~900 km³ of potential rhyolitic magma (Huang et al., 2015). However, magma mobility at an average melt fraction of only ~9% is limited by high viscosity due to abundant grain-to-grain contacts in mush with less than ~35–50% melt, often described as causing 'rheological lock-up' (Costa et al., 2009; Cashman et al., 2017). A similar total amount of magma, ~900–1400 km³, is inferred within a smaller, ~3300–6600 km³, middle-to-upper crustal reservoir beneath Long Valley caldera (Flinders et al., 2018). The higher, ~23%, average melt fraction inferred for the Long Valley reservoir places it below typical estimates of 'eruptible' magma, but closer to the dramatic decrease in

magma viscosity estimated to occur at melt fractions of ~35–50% (Costa et al., 2009). Beneath Valles caldera the middle-to-upper crustal magma reservoir is estimated to be much smaller, ~500 km³, and contain a minimum melt fraction of 10% or at least ~50 km³ of total magma distributed across the reservoir (Steck et al., 1998).

The magmatic volume estimates above should not be directly interpreted as the amount of magma immediately available to fuel the next potential eruption. The foremost reason is that the broadly distributed magma in the seismically imaged reservoirs or crystal-rich mush zones is unlikely to be completely concentrated into an eruptible reservoir (e.g., Marsh, 1981; Bachmann and Bergantz, 2004). Based on typical estimates of the intrusive/extrusive ratio and evidence for limited involvement of crystal-rich mushes such as glomerocrysts and cumulates in silicic eruptions (Bachmann and Huber, 2016; and references therein), it is more likely that only a fraction of the total seismically estimated magma volume would contribute to future eruptions. However, if even a small fraction of the ~900–1400 km³ of magma estimated for

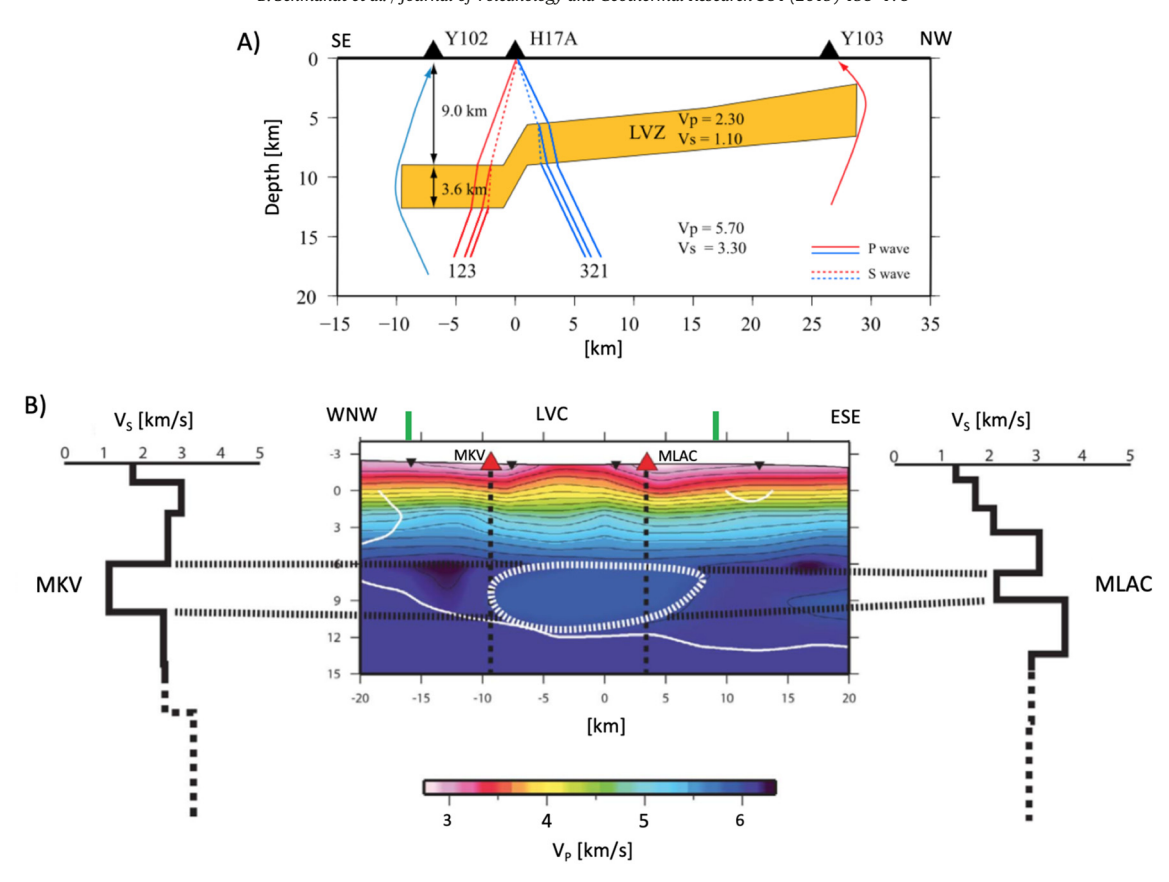


Fig. 8. Scattered wave and ray bending constraints on the Yellowstone and Long Valley magma reservoirs. A) The preferred model from a 2D full waveform forward modeling study of teleseismic P and forward scattered P-to-S waveforms modified from Chu et al., (2010). P-waves are shown with solid lines and S-waves are shown with dashed lines. Events originating in the southeast are shown in red and events from the northwest are shown in blue. The southeast to northwest cross-section is an idealized model as all the stations are not exactly aligned on a linear transect and the forward modeling sought to constrain the first-order waveform features for seismographs near the reservoir edges and interior, respectively. Anomalous ray bending for paths approaching Y102 and Y103 was identified reverse polarity radial component waveforms that require a sharp edge to an extremely low velocity zone (LVZ). P-to-S scattering identified with receiver function analysis above the reservoir interior at H17A constrained sharp upper and lower boundaries of the LVZ. B) Locally 1D receiver function inversions for V_S as a function of depth beneath two seismographs from Long Valley caldera are shown on opposite sides of a local earthquake P wave tomography image modified from Seccia et al., (2011). Velocities below -12 km are not well constrained due to the distribution of local earthquake and seismographs. The horizontal dashed lines denote the inferred depths of the LVZ based on the approximate consistency of both methods.

the middle-to-upper crustal reservoirs beneath Yellowstone and Long Valley calderas became concentrated into an eruptible reservoir it would be sufficient to supply VEI 7 eruptions.

Aspects of interpretation of seismic velocities in the context of magmatic system structure could also bias seismic estimates of the abundance and mobility of magma. For instance, the preceding magmatic volume estimates were derived without ability to distinguish between silicate melt and exsolved volatile phases, which may accumulate near the tops of these reservoirs and could lead to overestimates of the amount and concentration of silicic magma (e.g., Edmonds and Woods, 2018; Hildreth, 2017). Additionally, the estimates above were based on isotropic inversions using only one seismic wave type (P or Rayleigh). Internal organization of the magma reservoirs could create seismic anisotropy and bias melt estimates if melt is concentrated in structures like sill or dike complexes.

4.4. Seismically anisotropic magma reservoirs

The ability to extract Rayleigh and Love wave signals from ambient noise interferometry has recently enabled radially anisotropic surface wave tomography studies of magmatic systems (Jaxybulatov et al., 2014; Harmon and Rychert, 2015; Mordret et al., 2015; Jiang et al., 2018; Lynner et al., 2018). Radial anisotropy is defined here as 100%* (V_{SH}-V_{SV})/V_S, where V_S is the Voigt average of V_{SH} and V_{SV} (Babuska and Cara, 1991). It is a simplified form of anisotropy that is often referred to as transverse isotropy because it assumes hexagonal anisotropy with a

vertical symmetry axis so that vertically and horizontal polarized shear waves propagate at distinct speeds. Beneath Toba caldera, positive radial anisotropy indicating $V_{SH} > V_{SV}$ was found to extend to the maximum depth of resolution, which was ~20 km. Positive radial anisotropy suggests horizontal layering of heterogeneous seismic velocities, consistent with the interpretation of a magmatic sill complex (Jaxybulatov et al., 2014; Postma, 1955; Backus, 1962). The opposite form of radial anisotropy (negative radial anisotropy) with $V_{SV} > V_{SH}$ was detected at a mafic volcanic system, Piton de la Fournaise, and interpreted as a set of basaltic dikes (Mordret et al., 2015). The middle-to-upper crustal magma reservoirs beneath Yellowstone and Long Valley calderas both exhibit strong, ~10%, positive radial anisotropy (Fig. 9; Jiang et al., 2018a). At depths \gtrsim 20 km radial anisotropy is weaker and more uncertain, consistent with a change in the geometric distribution and/or abundance of magma in the lower crust (Jiang et al., 2018a).

Positive radial anisotropy in the middle-to-upper crustal magma reservoir provides evidence for horizontal layering, but a variety of sill complex structures may be able to satisfy the seismic constraints. In a 3D context, positive radial anisotropy reservoirs could be composed of laterally extensive sills or smaller scale structures such as many coin or disc shaped volumes of melt (Taylor and Singh, 2002). In a 1D context, the ratio of sills to intervening layers and the velocity contrast between the two are the key parameters. For sill thickness that are small relative to the seismic wavelengths (~10–30 km) there is negligible sensitivity to layer thickness (Jaxybulatov et al., 2014). There are trade-offs among the depth-averaged ratio of the crystal-poor and crystal-rich

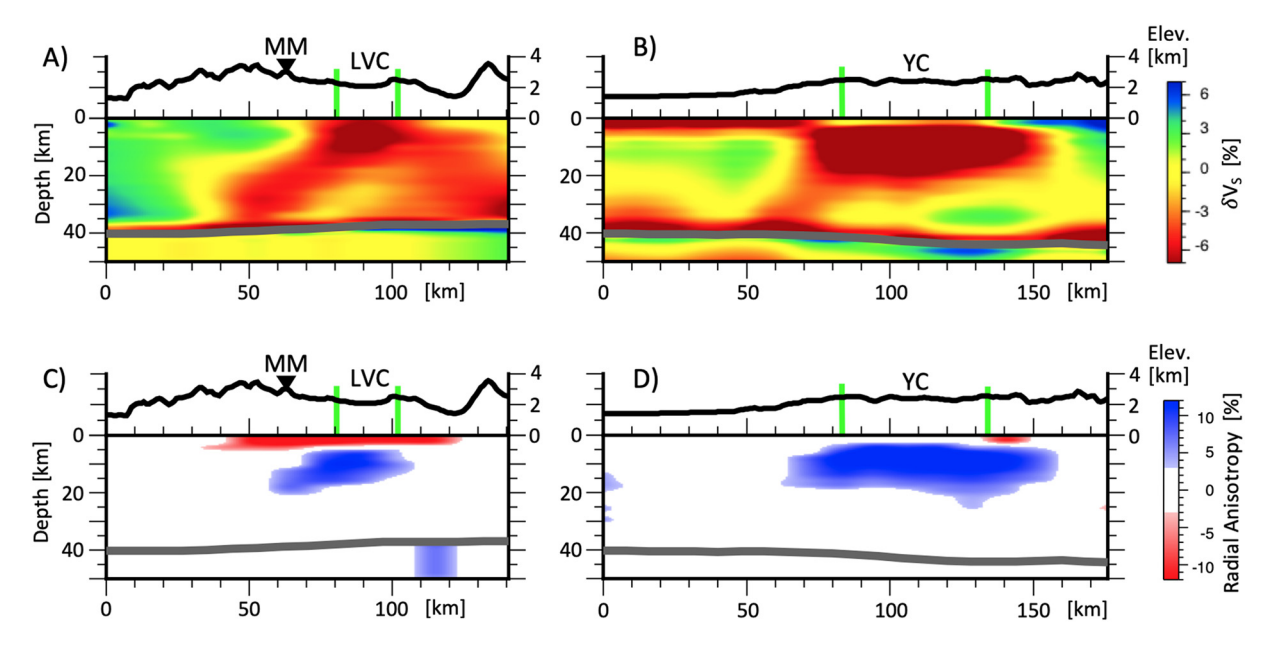


Fig. 9. Radial anisotropy beneath Long Valley and Yellowstone calderas. A) Cross-section of isotropic V_S perturbations for the A-A' transect across Long Valley caldera labeled in Fig. 1B. B) Cross-section of isotropic V_S perturbations for the B-B' transect across Yellowstone caldera labeled in Fig. 1C. C) Radial anisotropy cross-section for Long Valley. Following Jiang et al. (2018a) anisotropy is plotted where non-zero anisotropy is required at >95% confidence. D) Same as (C), but for the Yellowstone radial anisotropy cross-section. The locations of Long Valley caldera (LVC), Mammoth Mountain (MM), and Yellowstone caldera (YC) are labeled.

layers in the cumulative sill complex as well as the shear velocities (melt fractions) of the relatively crystal-poor and crystal-rich layers. To illustrate these tradeoffs, we use the anisotropic V_S profile beneath Yellowstone caldera from Jiang et al. (2018a) and the effective vertical transversely isotropic (VTI) modeling approach described by Jaxybulatov et al. (2014) and based on Postma, (1955) (Fig. 10). The method of Postma, (1955) was used to predict V_{SV} and V_{SH} for the tradeoff analysis. The structure of a magmatic sill complex was modeled as a stack of horizontally oriented relatively crystal-poor (lower V_S) and crystal-rich (higher V_S) layers, between 5 and 18 km depth (Jiang et al., 2018a). Each model in the grid search was evaluated by its misfit to the tomography results using the following equation:

$$\begin{split} \textit{Misfit} &= \left(\frac{\textit{V}_{\textit{SV}}(\textit{pre}) - \textit{V}_{\textit{SV}}(\textit{obs})}{0.1}\right)^2 + \left(\frac{\textit{V}_{\textit{SH}}(\textit{pre}) - \textit{V}_{\textit{SH}}(\textit{obs})}{0.1}\right)^2 \\ &\quad + \left(\frac{\textit{RA}(\textit{pre}) - \textit{RA}(\textit{obs})}{3}\right)^2 \end{split} \tag{1}$$

In Eq. (1), the observed values of V_{SV}, V_{SH}, and radial anisotropy (RA) are from the anisotropic tomography model of Jiang et al. (2018a) beneath the center of Yellowstone caldera. The best fits to the local Rayleigh and Love wave dispersion are for structures composed of 5-40% crystalpoor sills and 60-95% intervening crystal-rich layers. In this context the relatively crystal-poor layers would have ~35-50% low-V_S anomalies, which are comparable to those estimated by some scattered wave studies of the boundaries of middle-to-upper crustal magma reservoirs beneath Yellowstone and Long Valley calderas (Chu et al., 2010; Seccia et al., 2011). Further insights regarding intra-reservoir structures could be gained by 2D or 3D wave field modeling of hypothetical sill complexes, which would be considerably more computationally expensive. The simplified VTI calculations in the grid search should be considered as a tool to identify narrower parameter spaces worthy of further scrutiny. Radially anisotropic tomography results to date suggest that large velocity contrasts between approximately horizontal crystal-poor and crystal-rich layers are common features within tomographically inferred middle-toupper crustal magma reservoirs beneath Toba, Yellowstone, and Long Valley calderas (Jaxybulatov et al., 2014; Jiang et al., 2018a). It is unknown if the smaller magma reservoir inferred from P-wave tomography beneath Valles caldera is similarly anisotropic.

The propagating Yellowstone hotspot offers a rare opportunity to consider the temporal evolution of a radially anisotropic magma reservoir. The middle-to-upper crust beneath prior caldera complexes of the Yellowstone hotspot, ~5-16 Ma, exhibits weaker to negligible radial anisotropy compared to the modern reservoirs beneath Yellowstone and Long Valley calderas (Jiang et al., 2018a; Moschetti et al., 2010). Homogenization of seismic properties upon crystallization or drainage of the meltrich layers in eruptions could explain why radial anisotropy fades following the movement of the Yellowstone hotspot to a new silicic caldera complex (Jiang et al., 2018a). Construction of upper crustal silicic magma reservoirs as sill complexes is supported by a recent field mapping and geochronology study of a silicic fossil magma reservoir exhumed from ~7–8 km depth in the Coast Plutonic Complex of the northwestern U.S. Cordillera (Eddy et al., 2016). The exposed ~2 km depth interval includes 4 variable thickness sills emplaced within ~740 kyr, with the largest individual sill emplaced within ~26 kyr (Eddy et al., 2016). Creation of strongly heterogeneous seismic velocity structure with depth thus appears plausible as a result of geologically rapid emplacement of new sills into existing mush zones.

4.5. Uncertainty in seismic signatures of crustal magma

In the preceding sections the estimated melt fractions in the middle-to-upper silicic magma reservoirs were reported based on the inferences in the original seismic imaging studies as they reflect the authors' locally-specific estimates at the time of publication. Here we wish to illustrate the potential magnitude of uncertainty in crustal melt fraction estimates to highlight opportunities for continued interdisciplinary advancement. Constraints on the partial derivatives of seismic velocities with respect to silicate melt fraction are obtained from laboratory experiments (Askarpour et al., 1993; Schilling et al., 2003; Scheu et al., 2006; Caricchi et al., 2008; Clark et al., 2016) and theoretical models based on measured material properties and idealized melt distributions (Mavko, 1980; Schmeling, 1985; Taylor and Singh, 2002; Takei, 2002). Many laboratory experiments focus on measurements of silicate liquids and glasses, whereas others attempt to measure partially molten aggregates at different melt fractions (Caricchi et al., 2008). Applications of

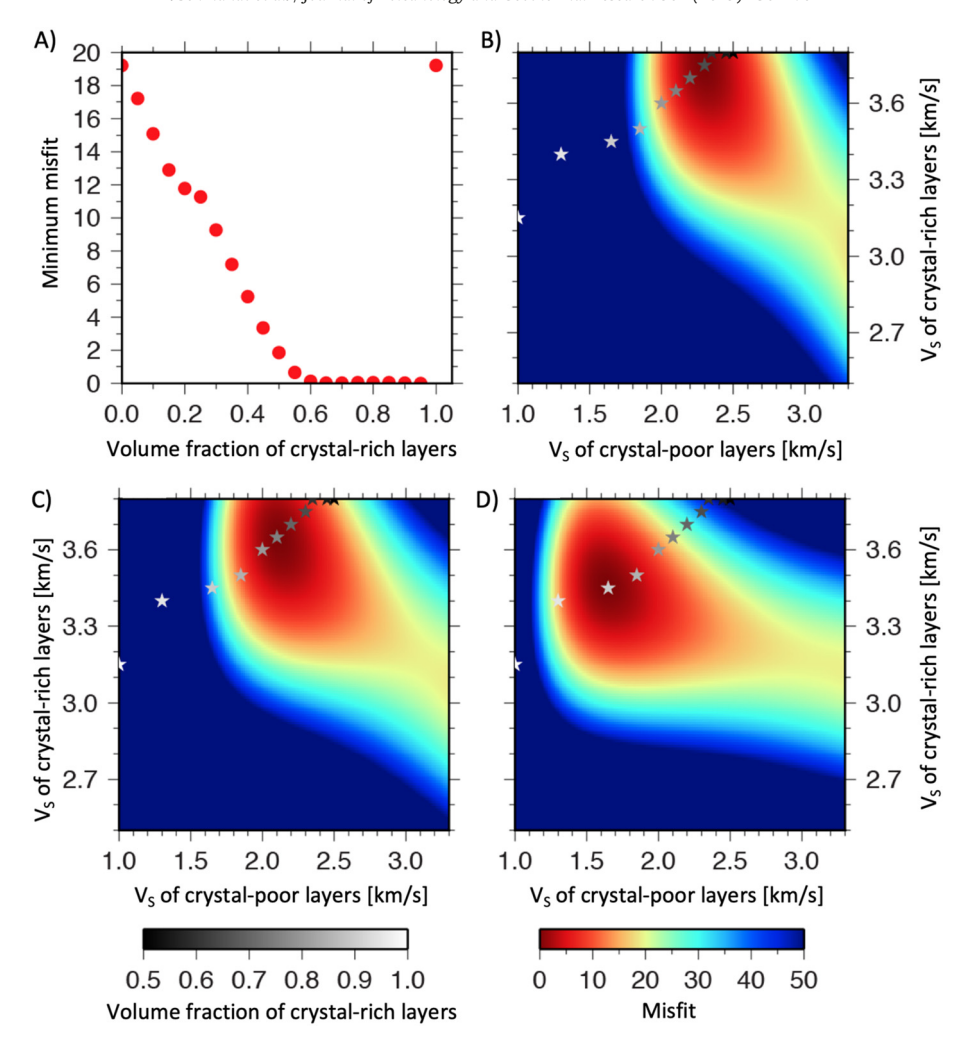


Fig. 10. Modeling results of potential configuration in the hypothesized sill complex using the seismic observations from Yellowstone. (a) The overall misfit variation as the volume fraction of relatively crystal-rich layers. (b–d) Misfit plots showing the trade-off of the shear-wave velocity between the relatively crystal-poor and crystal-rich layers for three different volume fractions of the crystal-rich layers: 65% (b), 75% (c) and 90% (d). The gray-filled stars represent the best fitting models for each volume fraction. Misfit is unitless because it combines misfit to absolute shear velocities and the percentage of anisotropy as shown in Eq. (1).

the experimental and theoretical results to seismic interpretations are challenged by the wide range of potential crustal magma compositions and the inherent difficulty of constraining the in-situ melt distribution, which likely varies with melt fraction and melt migration rates. Some commonly applied models for estimating silicic melt fractions based on seismic velocities are considered below.

As an example, we consider estimates of the V_S reduction per percent melt increase for melt fractions near ~15%, which we refer to as dV_S/df. This melt fraction is chosen because it is approximately in the middle of melt fractions estimated for the middle-to-upper crustal magma reservoirs considered in this review and it is well below the strongly non-linear dependence of V_S on melt fraction that occurs as the aggregate material transitions from an interconnected crystalline framework to crystals in suspension. Locally specific values include dV_S/df ≅ -23 m/s/% estimated for a rhyolitic reservoir beneath Long Valley caldera (Caricchi et al., 2008; Flinders et al., 2018) and $dV_s/df \approx -50 \text{ m/s/}\%$ estimated for the rhyolitic reservoir beneath Yellowstone caldera (Chu et al., 2010). One theoretical model suggests $dV_s/df \approx -100 \text{ m/s/\%}$ for rhyolitic melt assuming it is in triangular grain boundary tubes, although such an equilibrium distribution may only be relevant for low melt fractions and systems that are not being actively recharged (Watanabe, 1993). It is clear that the assumed geometry of melt volumes is a major source of variability among estimates of dV_S/df. Taylor and Singh (2002) report that dV_S/df can vary from 73 m/s/% for oblate spheroids with 10:1 aspect ratio to 30 m/s/% for spherical melt volumes. The total range of estimates considered above for dV_S/df for melt fractions near 15% is ~23 to -100 m/s/%. Models based on laboratory measurements at multiple melt fractions may offer a more realistic assessment of how the effects of melt-crystal contacts evolve with melt fraction for a given composition (e.g., Caricchi et al., 2008). However, existing laboratory studies using materials such as alumina crystals in silicate melt (Caricchi et al., 2008) or polycrystalline aggregates of borneol (McCarthy and Takei, 2011) may not be directly applicable to other partially molten aggregates in magma reservoirs with uncertain in-situ bulk and volatile compositions and evolving magma migration rates.

The range of models above corresponds to a factor of ~4 variation in potential melt fraction estimates, meaning that the $V_{\rm S}$ reduction needed to indicate 15% rhyolitic melt could vary from ~0.35–1.5 km/s compared to typical sub-solidus crustal $V_{\rm S}$. An additional concern based on the anisotropic structure of the middle-to-upper crustal reservoirs is that that spatially-averaged reservoir seismic properties may not accurately reflect the in-situ melt fractions if the reservoirs are composed of relatively crystal-rich and crystal-poor sub-volumes. While recent seismic estimates of the reservoir-averaged melt fractions at locations such as Yellowstone and Long Valley consider a variety of information including experimental and theoretical constraints of melt effects combined with local estimates of bulk and volatile composition (e.g., Chu et al., 2010; Huang et al., 2015; Flinders et al., 2018), there are large remaining sources of uncertainty that could impact seismic estimates of magma mobility and maximum feasible eruptive volumes.

5. Integrated magmatic system structure and links to volcanic life cycles

5.1. Potential origins of continued mantle melt supply

Evaluating the modern supply of upper mantle melt following 0.63–1.25 Ma caldera-forming silicic eruptions is pertinent because basaltic melt must be extracted from large volumes of upper mantle to fuel voluminous silicic magmatism. Assuming a plutonic/volcanic volume ratio of 5:1 and 5% melting of the upper mantle, mantle source volumes are a factor of ~100 greater than erupted silicic tuff volumes (Farmer et al., 2008). Following that estimate, on the order of ~100,000 km³ of mantle (~50 km cube), must be partially melted to fuel a ~1000 km³ silicic tuff, similar to the 0.63 Ma Lava Creek tuff from Yellowstone. Mantle source volumes would be even larger if higher intrusive/extrusive ratios or lower mantle melt fractions are considered.

Seismic tomography consistent with ongoing presence of upper mantle melt beneath the three calderas suggests rejuvenation of the mantle source regions and potential recharge of primitive melt input to the lower crust are likely since the last caldera-forming eruptions. Movement of the Yellowstone hotspot is a clear way to access mantle that is not melt-depleted so long as the cratonic lithospheric mantle is convectively thinned to allow upwelling across the dry solidus (e.g., Rigo et al., 2015; Colón et al., 2018). For Long Valley caldera the thin lithosphere of the Walker Lane (~55 km) and high transtensional strain rate for a plate interior may enable continued supply of mantle melt (Fig. 2D; Gazel et al., 2012; Kreemer et al., 2014; Kohlstedt and Holtzman, 2009). The evidence of modern mantle melt beneath Valles caldera is more ambiguous and it is not clear if asthenosphere can flow above the dry solidus beneath Valles caldera given that lithospheric thickness estimates are highly variable, ~60-100 km, at the transition from the Colorado Plateau to Rio Grande rift (Levander and Miller, 2012; Lekić and Fischer, 2014; Hansen et al., 2015). Also, the slow contemporary strain rates surrounding the Rio Grande rift may not focus melt ascent into the lithosphere as effectively as beneath higher strain rate regions such as the Walker Lane and Yellowstone Plateau (Fig. 2D; Berglund et al., 2012; Kreemer et al., 2014). Alternative mechanisms to enable melt input at the base of the crust include localized delamination and consequent upward return flow (e.g., Elkins-Tanton, 2007), which may not be detected if the lateral extent of destabilized mantle lithosphere is ≤70-km spacing of the TA.

5.2. Multi-stage crustal reservoirs

The seismic imaging constraints reviewed in Section 4 are consistent with the concept of multi-stage transcrustal magmatic systems that are dominated by crystal-rich mush rather than magma with isolated crystals in suspension (Cashman et al., 2017). Seismic tomography studies from Yellowstone, Long Valley, and Valles calderas suggest that major reservoirs in the lower and middle-to-upper crust with an intervening decrease in melt storage may be a common configuration for voluminous silicic transcrustal magmatic systems (Weiland et al., 1995; Huang et al., 2015; Steck et al., 1998). The clearest support for two major reservoirs with lower melt fractions at intervening depths comes from tomography including teleseismic body waves. Surface wave tomography studies yield highly consistent evidence for the middle-to-upper crustal reservoirs, but distinct lower crustal reservoirs imaged by surface wave tomography exhibit different geometries or less prominent velocity anomalies (Figs. 5 & 6; Jiang et al., 2018a; Flinders et al., 2018). Decreased model similarity at lower crustal depths may be an expression of lower melt fractions in the lower crust because weaker distortion of seismic wave fields would make the structures more difficult to consistently resolve with different data sets. Such an interpretation is consistent with mechanical modeling and zircon geochronology indicating that the upper-to-middle crustal depth interval can support long-term, up to ~10⁵ years, accumulation of neareruptible mush in large silicic magmatic systems (Gelman et al., 2013; de Silva and Gregg, 2014; Karakas et al., 2017; Costa, 2008; Cooper, 2019). The higher pressure and temperature conditions of the lower crust favor maintenance of lower melt fraction mafic reservoirs whose melts would be efficiently segregated and transported to shallower depths leaving highly crystalline cumulate mush behind (Annen et al., 2005; Solano et al., 2012). From a seismological perspective, greater variability of tomography results for the lower crust highlights the need to continue advancing the use of inversion methods that incorporate multiple wave types and enhance seismic array designs to provide broadband sensitivity throughout transcrustal magmatic systems.

Improved seismic resolution of the lower crustal components of magmatic systems and how they connect to their shallower counterparts would be beneficial for interdisciplinary studies of transcrustal magmatic system evolution and volcanic monitoring. For example, the first study to combine local and teleseismic earthquake data for crustal imaging around Yellowstone caldera identified a larger and lower melt fraction lower crustal reservoir beneath Yellowstone (Huang et al., 2015). That new insight regarding magmatic system structure supported subsequent formulation and testing of physical models for Yellowstone's transcrustal magmatic system across a range of time scales (Colón et al., 2018, 2019; Reuber et al., 2018). Thermomechanical modeling of hotspot evolution found that the depths, sizes, and contrasting melt fraction estimates for the seismically inferred magma reservoirs can be approximately predicted based on effects of the brittleductile transition on transcrustal melt transport (Colón et al., 2018). The modeled time-pressure-temperature paths of melts further provided a means to evaluate isotopic evolution of magmas for comparison with past eruptions (Colón et al., 2019). Aside from serving as a reference for forward models of magmatic systems, seismic images of transcrustal magmatic systems can inform geodynamic inversions based on adjoint modeling to estimate rheological parameters and inter-reservoir connectivity consistent with gravity and geodetic observations (Reuber et al., 2018). Efforts to interpret monitoring of volcanic gas emissions also benefit from constraints on the deep crustal components of magmatic systems because gas fluxes can be decoupled from silicate melt transport due to exsolution at depth and potential stalling at permeability boundaries in the upper crust (Lesne et al., 2011; Wallace et al., 1999; Wallace, 2005; Edmonds and Woods, 2018). Consequently, seismic constraints on the depths and volumes of multi-stage magma reservoirs can aid in understanding volatile budgets that appear infeasible based on upper crustal magmatic reservoirs alone (e.g., Huang et al., 2015).

5.3. Links to prior rhyolitic magma reservoirs and volcanic life-cycles

Geochronology of resilient zircon and sanidine crystal suggests that differentiation of voluminous rhyolites typically occurs over time scales of 10³–10⁵ years in crystal-rich middle-to-upper crustal magma reservoirs (Costa, 2008; Cooper, 2019), but large eruptions are fueled by shorter-lived crystal-poor reservoirs (e.g., Stelten et al., 2015). Different silicic volcanic fields and different eruptions from the same caldera complex exhibit variable residence time estimates. For instance, estimates from the Yellowstone caldera complex indicate ~35 kyr for the 0.63 Ma Lava Creek tuff (Matthews et al., 2015) and longer, ~150-250 kyr, crystallization intervals for smaller post-caldera eruptions (Stelten et al., 2015). In some cases, a small fraction of zircons may define a longer total range while most were crystallized in a shorter period of time. For example, the Bishop tuff-forming magma reservoir may have hosted zircon crystallization over a total time span of ~80 kyr (Chamberlain et al., 2013), but most analyzed zircons crystallized within only ~5 kyr (Crowley et al., 2007). Combined zircon and sanidine geochronology of the Lava Creek tuff suggests that rhyolitic melts were quickly extracted from a longer-lived, ~35 kyr, crystal-rich reservoir and transported to a shorter-lived, ≤1 kyr, crystal-poor reservoir (Stelten et al., 2015). The potential for long-lived crystal-rich magma reservoirs makes the possibility of finding seismic evidence for modern magma reservoirs beneath all three calderas plausible in the context of past volcanic cycles. Additionally, a highly ephemeral presence of crystal-poor reservoirs is consistent with the scarcity of seismic evidence for voluminous magma reservoirs with low enough crystal content to completely block shear waves (e.g., Pritchard and Gregg, 2016).

The conceptual model of long-lived crystal-rich reservoirs quickly giving rise to shorter-lived eruptible reservoirs demands a framework for melt organization that can enable accumulation for long periods of time and then quickly become unstable (Cashman et al., 2017). Geochemical support for such a model comes from identification of trace element and isotopic compositional heterogeneity in tuffs from the three volcanic systems that are inconsistent with long-term storage in a single well-mixed crystal-poor reservoir (Wotzlaw et al., 2015; Matthews et al., 2015; Myers et al., 2016; Ellis and Wolff, 2012; Befus and Gardner, 2016; Swallow et al., 2018; Roberge et al., 2013; Gualda and Ghiorso, 2013; Wolff and Ramos, 2013). Seismic evidence for locally heterogeneous melt fractions based on radial anisotropy consistent with layering of relatively crystal-poor and crystal-rich volumes beneath Yellowstone and Long Valley calderas may provide hints regarding the reservoir structure that maintains trace element and isotopic heterogeneity before large eruptions (Fig. 9; Jiang et al., 2018a). If melt in the long-lived reservoirs is largely isolated in subset volumes, such as sills or lenses, within the cumulative reservoirs then in-situ melt fractions would be higher than expected based on reservoir average melt fractions and in-situ effective viscosities would be lower (Jiang et al., 2018a). Extraction of the crystal-poor rhyolite fraction could then result from a climactic recharge event that increases connectivity between low-viscosity magmas stored in distinct sills allowing large eruptions to tap multiple batches of crystal-poor rhyolite that have insufficient time to completely homogenize (Cashman and Giordano, 2014; Wotzlaw et al., 2015).

The time-scales of the final recharge events that could destabilize long-lived reservoirs and concentrate magma in crystal-poor eruptible reservoirs have been the subject of considerable geochemical research and debate in recent years. Measurement and modeling of diffusion profiles of zoned crystals, referred to as 'diffusion chronometry', suggests that the final magmatic recharge and melting events leading to eruptible crystal-poor reservoirs of silicic magma may take place over time scales as short as months to centuries at Yellowstone and Long Valley calderas (Till et al., 2015; Rubin et al., 2017; Chamberlain et al., 2014; Wark et al., 2007; Shamloo and Till, 2019). Uncertainties regarding different crystal clocks, diffusion coefficients, and interpretations of the resulting time scales in terms of specific pre-eruption processes motivate debate about recent diffusion chronometry results (e.g., Wilson et al., 2017; de León and Schmitt, 2019; Cooper, 2019). However, the emerging perspective from diffusion chronometry studies remains that long-lived, 10³-10⁵ years, crystal-rich reservoirs are rapidly destabilized and the resulting crystal-poor eruptible reservoirs persist for only a small fraction of those time scales making them less likely to be observed in the modern snapshots provided by seismic imaging. In contrast to the three silicic magmatic systems reviewed here, recent geophysical evidence indicates a shallower ~2–8 km deep silicic reservoir beneath the Laguna del Maule volcanic field in the Andes (Wespestad et al., 2019). This may be a rare case where it is possible to observe the structure of a large silicic magmatic system while it is in the potentially eruptible phase of its life-cycle.

6. Summary and future opportunities

Seismic imaging of magmatic systems underlying Yellowstone, Long Valley, and Valles calderas supports the concept of integrative investigation of magmatic systems from their primitive upper mantle inputs to their likely short-lived eruptible reservoirs of crystal-poor silicic magma. Not all aspects of magmatic system evolution are captured by

modern seismic imaging of a few systems but important insights into their life-cycles can be gained. Continued supply of upper mantle melt since the 0.63–1.25 Ma caldera-forming eruptions is likely, particularly beneath Yellowstone and Long Valley calderas where upper mantle seismic velocities are similar to or lower than those estimated beneath mid-ocean spreading ridges. Seismic tomography finds some evidence for lower crustal reservoirs beneath all three calderas, but their velocity anomalies are generally subtler than middle-to-upper crustal reservoirs and their geometry is more variable between different types of seismic imaging suggesting a need for continued improvement of seismic imaging in this depth range. Middle-to-upper crustal magma reservoirs are prominent seismic features beneath all three calderas at ~5-15 km depth. Scattered wave or ray-bending evidence suggests the reservoirs have sharp edges and strongly reduced velocities. Estimates of total melt content in the three reservoirs vary from ~50–1400 km³. The average melt fraction estimates of ~9-23% indicate that the existing melts would likely need to be reorganized and concentrated to form large eruptible reservoirs. Positive radial anisotropy beneath Yellowstone and Long Valley calderas highlights the possibility that pre-eruptive magma reservoir reorganization could occur by rapidly connecting sills and concentrating their crystal-poor contents in short-lived eruptible reservoirs. Outstanding challenges include improved multi-scale characterization of magma reservoir melt fractions and the architecture of intra-reservoir structures, such as sill complexes, that may be critical to linking physical and chemical models of how long-lived magma reservoirs transition into eruptible reservoirs.

Future opportunities for advancing seismic constraints on magmatic system structure generally demand inversion frameworks that can assimilate and accurately model diverse body and surface wave measurements, in addition to seismic survey designs that provide multiple types of seismic sampling from primitive melt inputs to the top of the magmatic system. Full waveform inversion approaches using complete 3D forward modeling of the seismic wave field are an important direction for advancement, because they can naturally accommodate broadband surface and P & S body wave measurements that are more often used separately (Yuan and Simons, 2014; Yuan et al., 2015). However, simpler and more computationally efficient joint inversions of measurements from multiple wave types continue to provide valuable new insights into magmatic system structures (e.g., Ward et al., 2014; Koulakov et al., 2009). Efficient approaches using assumptions such as ray theory or locally 1D wave propagation are also useful as preliminary steps toward computationally challenging waveform tomography, because moderately accurate 3D starting models are beneficial for highfrequency waveform inversions (Virieux and Operto, 2009). Another exciting direction for advance is increased use of time-dependent monitoring of velocity structure through seismic coda wave interferometry, which can potentially detect small fractional changes in velocity structure associated with evolution of the magmatic system (Brenguier et al., 2008, 2016). In cases of major changes in subsurface activity, time-dependent structure may also be constrained by repeated tomography studies (e.g., Koulakov et al., 2013; Julian and Foulger, 2010).

Improved methodological approaches must be coupled with ambitious seismic survey designs as dense sampling is needed to constrain features such as sharply defined 3D interfaces and anisotropic volumes. Additionally, wide arrays (>50 km) are needed (at least temporarily) to obtain body and surface wave sampling throughout transcrustal continental magmatic systems. An encouraging recent example is the imaging Magma Under mt. St. Helens (iMUSH) project, which included nested arrays of ~70 broadband and >3000 rapidly deployable short period seismometers for combined natural and controlled source imaging (Kiser et al., 2016, 2018; Mann et al., 2019; Han et al., 2018; Hansen et al., 2016; Hansen and Schmandt, 2015). Such deployments of large numbers of continuously recording seismographs are increasingly feasible with modern cable-free instruments initially developed for resource exploration (e.g., Lin et al., 2013; Schmandt and Clayton, 2013). Further use of hybrid natural and controlled source seismic surveys is well

suited to scrutinizing large silicic magmatic system structure at high frequencies while still providing shear wave information and lower frequencies that are beneficial for stabilizing full waveform tomography and estimating physical properties throughout the crust and upper mantle.

Advanced seismic imaging results should be integrated with a broad suite of geophysical and geochemical constraints to improve systematic understanding of large silicic magmatic systems. Complementary insights from earthquake seismology, magnetotelluric imaging, gravimetry, and geodesy can aid interpretations of magmatic system structures by identifying contemporary subsurface deformation and helping distinguish variable composition magma reservoirs and hydrothermal systems (e.g., Pritchard et al., 2018; Wespestad et al., 2019). Additionally, geochemical and petrological studies of past eruptions and ongoing gas emissions provide insight into the likely bulk and volatile compositions of seismically imaged contemporary magma reservoirs. Estimates of composition are needed to identify the range of locally suitable scaling relationships between seismic velocities and melt fractions. Finally, further advances are needed in experimental and theoretical constraints on the scaling relationships between seismic parameters and the wide range of partially molten crustal rocks and magmatic volatile phases in actively evolving magmatic systems from the upper mantle to the upper crust.

Acknowledgements

The authors appreciate the encouragement and invitation from the journal editors to write this review, and thank an anonymous reviewer, Cliff Thurber, and the editor for their helpful feedback. Many collaborators and colleagues contributed to research results and discussions that positively influenced the manuscript. Ashton Flinders and Hsin-Hua Huang generously provided modified figures. Claudia Aprea provided information about seismic array data for Valles caldera. NSF grant EAR-1554908 supported related research and synthesis efforts.

References

- Afonso, J.C., Ranalli, G., Fernàndez, M., Griffin, W.L., O'Reilly, S.Y., Faul, U., 2010. On the Vp/ Vs-Mg# correlation in mantle peridotites: Implications for the identification of thermal and compositional anomalies in the upper mantle. Earth Planet. Sci. Lett. 289 (3-4), 606–618.
- Anders, M.H., Sleep, N.H., 1992. Magmatism and extension: the thermal and mechanical effects of the Yellowstone hotspot. Journal of Geophysical Research: Solid Earth 97 (B11), 15379–15393.
- Andersen, N.L., Jicha, B.R., Singer, B.S., Hildreth, W., 2017. Incremental heating of Bishop Tuff sanidine reveals preeruptive radiogenic Ar and rapid remobilization from cold storage. Proc. Natl. Acad. Sci. 114 (47), 12407–12412.
- Ankeny, L.A., Braile, L.W., Olsen, K.H., 1986. Upper crustal structure beneath the Jemez Mountains volcanic field, New Mexico, determined by three-dimensional simultaneous inversion of seismic refraction and earthquake data. Journal of Geophysical Research: Solid Earth 91 (B6), 6188–6198.
- Annen, C., Blundy, J.D., Sparks, R.S.J., 2005. The genesis of intermediate and silicic magmas in deep crustal hot zones. J. Petrol. 47 (3), 505–539.
- Aprea, C. M., Hildebrand, S., Fehler, M., Steck, L., Baldridge, W. S., Roberts, P., Thurber, C.H., & Lutter, W. J. (2002). Three-dimensional Kirchhoff migration: Imaging of the Jemez volcanic field using teleseismic data. *Journal of Geophysical Research: Solid Earth*, 107 (B10). ESE-11.
- Armstrong, R. L., Leeman, W. P., & Malde, H. E. (1975). K-Ar dating quaternary and Neogene volcanic rocks of the Snake River Plain, Idaho. *Am. J. Sci.*; (United States), 275(3).
- Askarpour, V., Manghnani, M.H., Richet, P., 1993. Elastic properties of diopside, anorthite, and grossular glasses and liquids: a Brillouin scattering study up to 1400 K. Journal of Geophysical Research: Solid Earth 98 (B10), 17683–17689.
- Atwater, T., 1970. Implications of plate tectonics for the Cenozoic tectonic evolution of western North America. Geol. Soc. Am. Bull. 81 (12), 3513–3536.
- Atwater, T., Stock, J., 1998. Pacific-North America plate tectonics of the Neogene southwestern United States: an update. Int. Geol. Rev. 40 (5), 375–402.
- Babuska, V., & Cara, M. (1991). Seismic anisotropy in the Earth (Vol. 10). Springer Science & Business Media.
- Bachmann, O., Huber, C., 2016. Silicic magma reservoirs in the Earth's crust. Am. Mineral. 101 (11), 2377–2404.
- Bailey, R.A., Dalrymple, G.B., Lanphere, M.A., 1976. Volcanism, structure, and geochronology of long valley caldera, mono county, California. J. Geophys. Res. 81 (5), 725–744.

- Barmin, M.P., Ritzwoller, M.H., Levshin, A.L., 2001. A Fast and Reliable Method for Surface Wave Tomography. In *Monitoring the Comprehensive Nuclear-Test-Ban Treaty: Surface Waves* (Pp. 1351–1375)Birkhäuser, Basel.
- Battaglia, M., Roberts, C., Segall, P., 1999. Magma intrusion beneath Long Valley caldera confirmed by temporal changes in gravity. Science 285 (5436), 2119–2122.
- Befus, K.S., Gardner, J.E., 2016. Magma storage and evolution of the most recent effusive and explosive eruptions from Yellowstone Caldera. Contrib. Mineral. Petrol. 171 (4), 30.
- Bennett, R.A., Wernicke, B.P., Niemi, N.A., Friedrich, A.M., Davis, J.L., 2003. Contemporary strain rates in the northern Basin and Range province from GPS data. Tectonics 22 (2).
- Benz, H.M., Smith, R.B., 1984. Simultaneous inversion for lateral velocity variations and hypocenters in the Yellowstone region using earthquake and refraction data. J. Geophys. Res. Solid Earth 89 (B2), 1208–1220.
- Berglund, H.T., Sheehan, A.F., Murray, M.H., Roy, M., Lowry, A.R., Nerem, R.S., Blume, F., 2012. Distributed deformation across the Rio Grande rift, Great Plains, and Colorado plateau. Geology 40 (1), 23–26.
- Borisov, D., Modrak, R., Gao, F., Tromp, J., 2017. 3D elastic full-waveform inversion of surface waves in the presence of irregular topography using an envelope-based misfit function. Geophysics 83 (1), R1–R11.
- Bostock, M.G., Rondenay, S., 1999. Migration of scattered teleseismic body waves. Geophys. J. Int. 137 (3), 732–746.
- Brenguier, F., Shapiro, N.M., Campillo, M., Nercessian, A., Ferrazzini, V., 2007. 3-D surface wave tomography of the Piton de la Fournaise volcano using seismic noise correlations. Geophys. Res. Lett. 34 (2).
- Brenguier, F., Shapiro, N.M., Campillo, M., Ferrazzini, V., Duputel, Z., Coutant, O., Nercessian, A., 2008. Towards forecasting volcanic eruptions using seismic noise. Nat. Geosci. 1 (2), 126.
- Brenguier, F., Rivet, D., Obermann, A., Nakata, N., Boué, P., Lecocq, T., Campillo, M., Shapiro, N., 2016. 4-D noise-based seismology at volcanoes: ongoing efforts and perspectives. J. Volcanol. Geotherm. Res. 321, 182–195.
- Burdick, S., van der Hilst, R.D., Vernon, F.L., Martynov, V., Cox, T., Eakins, J., Karasu, G.H., Tylell, J., Astiz, L., Pavlis, G.L., 2010. Model update January 2010: Upper mantle heterogeneity beneath North America from traveltime tomography with global and USArray Transportable Array data. Seismol. Res. Lett. 81 (5), 689–693.
- Busby, C.J., 2013. Birth of a plate boundary at ca. 12 Ma in the Ancestral Cascades arc. Walker Lane belt of California and Nevada. *Geosphere* 9 (5), 1147–1160.
- Camp, V.E., Ross, M.E., 2004. Mantle dynamics and genesis of mafic magmatism in the intermontane Pacific Northwest. Journal of Geophysical Research: Solid Earth 109 (B8).
- Camp, V.E., Pierce, K.L., Morgan, L.A., 2015. Yellowstone plume trigger for Basin and Range extension, and coeval emplacement of the Nevada–Columbia Basin magmatic belt. Geosphere 11 (2), 203–225.
- Caricchi, L., Burlini, L., Ulmer, P., 2008. Propagation of P and S-waves in magmas with different crystal contents: Insights into the crystallinity of magmatic reservoirs. J. Volcanol. Geotherm. Res. 178 (4), 740–750.
- Cashman, K.V., Giordano, G., 2014. Calderas and magma reservoirs. J. Volcanol. Geotherm. Res. 288, 28–45.
- Cashman, K. V., Sparks, R. S. J., & Blundy, J. D. (2017). Vertically extensive and unstable magmatic systems: a unified view of igneous processes. *Science*, 355(6331), eaag 3055.
- Chamberlain, K.J., Wilson, C.J., Wooden, J.L., Charlier, B.L., Ireland, T.R., 2013. New perspectives on the Bishop Tuff from zircon textures, ages and trace elements. J. Petrol. 55 (2), 395–426.
- Chamberlain, K.J., Morgan, D.J., Wilson, C.J., 2014. Timescales of mixing and mobilisation in the Bishop Tuff magma body: perspectives from diffusion chronometry. Contrib. Mineral. Petrol. 168 (1), 1034.
- Chang, W.L., Smith, R.B., Wicks, C., Farrell, J.M., Puskas, C.M., 2007. Accelerated uplift and magmatic intrusion of the Yellowstone caldera, 2004 to 2006. Science 318 (5852), 952–956
- Chang, W.L., Smith, R.B., Farrell, J., Puskas, C.M., 2010. An extraordinary episode of Yellowstone caldera uplift, 2004–2010, from GPS and InSAR observations. Geophys. Res. Lett. 37 (23).
- Chaput, J.A., Zandomeneghi, D., Aster, R.C., Knox, H., Kyle, P.R., 2012. Imaging of Erebus volcano using body wave seismic interferometry of Strombolian eruption coda. Geophys. Res. Lett. 39 (7).
- Christiansen, R. L. (2001), The Quaternary and Pliocene Yellowstone Plateau Volcanic Field of Wyoming, Idaho, and Montana, *U.S. Geol. Surv. Prof. Pap.* 729-*G*, U.S. Gov. Print. Off., Washington, D. C.
- Christiansen, R.L., Foulger, G.R., Evans, J.R., 2002. Upper-mantle origin of the Yellowstone hotspot. Geol. Soc. Am. Bull. 114 (10), 1245–1256.
- Christiansen, R.L., Lowenstern, J.B., Smith, R.B., Heasler, H., Morgan, L.A., Nathenson, M., Mastin, L.G., Muffler, L., Robinson, J.E., 2007. Preliminary Assessment of Volcanic and Hydrothermal Hazards in Yellowstone National Park and Vicinity. U. S, Geological Survey.
- Chu, R., Helmberger, D.V., Sun, D., Jackson, J.M., Zhu, L., 2010. Mushy magma beneath Yellowstone. Geophys. Res. Lett. 37 (1).
- Clark, A.N., Lesher, C.E., Jacobsen, S.D., Wang, Y., 2016. Anomalous density and elastic properties of basalt at high pressure: Reevaluating of the effect of melt fraction on seismic velocity in the Earth's crust and upper mantle. Journal of Geophysical Research: Solid Earth 121 (6), 4232–4248.
- Cline II, C.J., Faul, U.H., David, E.C., Berry, A.J., Jackson, I., 2018. Redox-influenced seismic properties of upper-mantle olivine. Nature 555 (7696), 355.
- Colgan, J.P., Henry, C.D., 2009. Rapid middle Miocene collapse of the Mesozoic orogenic plateau in north-Central Nevada. Int. Geol. Rev. 51 (9–11), 920–961.

- Colón, D.P., Bindeman, I.N., Gerya, T.V., 2018. Thermomechanical modeling of the formation of a multilevel, crustal-scale magmatic system by the Yellowstone plume. Geophys. Res. Lett. 45 (9), 3873–3879.
- Colón, D.P., Bindeman, I.N., Gerya, T.V., 2019. Understanding the isotopic and chemical evolution of Yellowstone hot spot magmatism using magmatic-thermomechanical modeling. I. Volcanol. Geotherm. Res. 370, 13–30.
- Cook, G.W., Wolff, J.A., Self, S., 2016. Estimating the eruptive volume of a large pyroclastic body: the Otowi Member of the Bandelier Tuff, Valles caldera, New Mexico. Bull. Volcanol. 78 (2), 10.
- Cooper, K.M., 2019. Time scales and temperatures of crystal storage in magma reservoirs: implications for magma reservoir dynamics. Phil. Trans. R. Soc. A 377 (2139), 20180009
- Costa, A., Caricchi, L., Bagdassarov, N., 2009. A model for the rheology of particle-bearing suspensions and partially molten rocks. Geochem. Geophys. Geosyst. 10 (3).
- Costa, F., 2008. Residence times of silicic magmas associated with calderas. Developments in volcanology 10, 1–55.
- Crosweller, H.S., Arora, B., Brown, S.K., Cottrell, E., Deligne, N.I., Guerrero, N.O., Hobbs, L., Kiyosugi, K., Loughlin, S.C., Lowndes, J., Nayembil, M., 2012. Global database on large magnitude explosive volcanic eruptions (LaMEVE). J. Appl. Volcanol. 1 (1), 4.
- Crowley, J.L., Schoene, B., Bowring, S.A., 2007. U-Pb dating of zircon in the Bishop Tuff at the millennial scale. Geology 35 (12), 1123–1126.
- Dalton, C.A., Faul, U.H., 2010. The oceanic and cratonic upper mantle: Clues from joint interpretation of global velocity and attenuation models. Lithos 120 (1–2), 160–172.
- Dawson, P.B., Evans, J.R., Iyer, H.M., 1990. Teleseismic tomography of the compressional wave velocity structure beneath the Long Valley region, California. Journal of Geophysical Research: Solid Earth 95 (B7), 11021–11050.
- De Siena, L., Thomas, C., Waite, G.P., Moran, S.C., Klemme, S., 2014. Attenuation and scattering tomography of the deep plumbing system of Mount St. Helens. *Journal of Geophysical Research: Solid Earth* 119 (11), 8223–8238.
- Deligne, N.I., Coles, S.G., Sparks, R.S.J., 2010. Recurrence rates of large explosive volcanic eruptions. Journal of Geophysical Research: Solid Earth 115 (B6).
- Dickinson, W.R., Snyder, W.S., 1979. Geometry of subducted slabs related to San Andreas transform. The Journal of Geology 87 (6), 609–627.
- Dreger, D.S., Tkalčić, H., Johnston, M., 2000. Dilational processes accompanying earthquakes in the Long Valley Caldera. Science 288 (5463), 122–125.
- Eddy, M.P., Bowring, S.A., Miller, R.B., Tepper, J.H., 2016. Rapid assembly and crystallization of a fossil large-volume silicic magma chamber. Geology 44 (4), 331–334.
- Edmonds, M., Woods, A.W., 2018. Exsolved volatiles in magma reservoirs. J. Volcanol. Geotherm. Res. 368, 13–30.
- Elkins-Tanton, L.T., 2007. Continental magmatism, volatile recycling, and a heterogeneous mantle caused by lithospheric gravitational instabilities. Journal of Geophysical Research: Solid Earth 112 (B3).
- Ellis, B.S., Wolff, J.A., 2012. Complex storage of rhyolite in the central Snake River Plain. J. Volcanol. Geotherm. Res. 211, 1–11.
- Farmer, G.L., Bailley, T., Elkins-Tanton, L.T., 2008. Mantle source volumes and the origin of the mid-Tertiary ignimbrite flare-up in the southern Rocky Mountains, western US. Lithos 102 (1–2), 279–294.
- Farrell, J., Smith, R.B., Taira, T.A., Chang, W.L., Puskas, C.M., 2010. Dynamics and rapid migration of the energetic 2008–2009 Yellowstone Lake earthquake swarm. Geophys. Res. Lett. 37 (19).
- Farrell, J., Smith, R.B., Husen, S., Diehl, T., 2014. Tomography from 26 years of seismicity revealing that the spatial extent of the Yellowstone crustal magma reservoir extends well beyond the Yellowstone caldera. Geophys. Res. Lett. 41 (9), 3068–3073.
- Faul, U.H., Jackson, I., 2005. The seismological signature of temperature and grain size variations in the upper mantle. Earth Planet. Sci. Lett. 234 (1–2), 119–134.
- Faulds, J.E., Henry, C.D., Spencer, J.E., Titley, S.R., 2008. Tectonic influences on the spatial and temporal evolution of the Walker Lane: an incipient transform fault along the evolving Pacific-North American plate boundary. Ores and orogenesis: Circum-Pacific tectonics, geologic evolution, and ore deposits: Arizona Geological Society Digest 22, 437–470.
- Faulds, J.E., Hinz, N., Kreemer, C., Coolbaugh, M., 2012. Regional patterns of geothermal activity in the Great Basin Region, Western USA: correlation with strain rates. Geothermal Resources Council Transactions 36, 897–902.
- Fenneman, N.M., 1917. Physiographic subdivision of the United States. Proc. Natl. Acad. Sci. U. S. A. 3 (1), 17.
- Flinders, A.F., Shen, Y., 2017. Seismic evidence for a possible deep crustal hot zone beneath Southwest Washington. Sci. Rep. 7 (1), 7400.
- Flinders, A.F., Shelly, D.R., Dawson, P.B., Hill, D.P., Tripoli, B., Shen, Y., 2018. Seismic evidence for significant melt beneath the Long Valley Caldera, California, USA. Geology 46 (9), 799–802.
- Forsyth, D.W., Scheirer, D.S., 1998. Imaging the deep seismic structure beneath a midocean ridge: the MELT experiment. Science 280 (5367), 1215–1220.
- Foulger, G.R., Julian, B.R., Pitt, A.M., Hill, D.P., Malin, P.E., Shalev, E., 2003. Three-dimensional crustal structure of Long Valley caldera, California, and evidence for the migration of CO2 under Mammoth Mountain. Journal of Geophysical Research: Solid Earth 108 (B3).
- Foulger, G.R., Julian, B.R., Hill, D.P., Pitt, A.M., Malin, P.E., Shalev, E., 2004. Non-double-couple microearthquakes at Long Valley caldera, California, provide evidence for hydraulic fracturing. J. Volcanol. Geotherm. Res. 132 (1), 45–71.
- Frassetto, A.M., Zandt, G., Gilbert, H., Owens, T.J., Jones, C.H., 2011. Structure of the Sierra Nevada from receiver functions and implications for lithospheric foundering. Geosphere 7 (4), 898–921.
- Gazel, E., Plank, T., Forsyth, D.W., Bendersky, C., Lee, C.T.A., Hauri, E.H., 2012. Lithosphere versus asthenosphere mantle sources at the big Pine Volcanic Field, California. Geochem. Geophys. Geosyst. 13 (6).

- Gelman, S.E., Gutiérrez, F.J., Bachmann, O., 2013. On the longevity of large upper crustal silicic magma reservoirs. Geology 41 (7), 759–762.
- Gilbert, F., Knopoff, L., 1960. Seismic scattering from topographic irregularities. J. Geophys. Res. 65 (10), 3437–3444.
- Gilbert, H., Yang, Y., Forsyth, D.W., Jones, C.H., Owens, T.J., Zandt, G., Stachnik, J.C., 2012. Imaging lithospheric foundering in the structure of the Sierra Nevada. Geosphere 8 (6) 1310–1330
- Goff, F., Gardner, J.N., Reneau, S.L., Kelley, S.A., Kempter, K.A., Lawrence, J.R., 2011. Geologic map of the Valles caldera, Jemez Mountains. New Mexico. *New Mexico Bur Geol Min Res Geol Map* 79.
- Graham, D.W., Reid, M.R., Jordan, B.T., Grunder, A.L., Leeman, W.P., Lupton, J.E., 2009. Mantle source provinces beneath the northwestern USA delimited by helium isotopes in young basalts. J. Volcanol. Geotherm. Res. 188 (1–3), 128–140.
- Gualda, G.A., Ghiorso, M.S., 2013. The Bishop Tuff giant magma body: an alternative to the Standard Model. Contrib. Mineral. Petrol. 166 (3), 755–775.
- Hammond, W.C., Humphreys, E.D., 2000. Upper mantle seismic wave velocity: Effects of realistic partial melt geometries. Journal of Geophysical Research: Solid Earth 105 (B5), 10975–10986.
- Hammond, W.C., Thatcher, W., 2004. Contemporary tectonic deformation of the Basin and Range province, western United States: 10 years of observation with the Global Positioning System. Journal of Geophysical Research: Solid Earth 109 (B8).
- Han, J., Vidale, J.E., Houston, H., Schmidt, D.A., Creager, K.C., 2018. Deep Long-Period Earthquakes beneath Mount St. Helens: their Relationship to Tidal stress, Episodic Tremor and Slip, and regular Earthquakes. Geophys. Res. Lett. 45 (5) 2241–2247
- Hansen, S.M., Schmandt, B., 2015. Automated detection and location of microseismicity at Mount St. Helens with a large-N geophone array. Geophys. Res. Lett. 42 (18), 7390-7397
- Hansen, S.M., Schmandt, B., 2017. P and S wave receiver function imaging of subduction with scattering kernels. Geochem. Geophys. Geosyst. 18 (12), 4487–4502.
- Hansen, S.M., Dueker, K., Schmandt, B., 2015. Thermal classification of lithospheric discontinuities beneath USArray. Earth Planet. Sci. Lett. 431, 36–47.
- Hansen, S.M., Schmandt, B., Levander, A., Kiser, E., Vidale, J.E., Abers, G.A., Creager, K.C., 2016. Seismic evidence for a cold serpentinized mantle wedge beneath Mount St Helens. Nat. Commun. 7, 13242.
- Harmon, N., Rychert, C.A., 2015. Seismic imaging of deep crustal melt sills beneath Costa Rica suggests a method for the formation of the Archean continental crust. Earth Planet. Sci. Lett. 430, 140–148.
- Harmon, N., Forsyth, D.W., Weeraratne, D.S., 2009. Thickening of young Pacific lithosphere from high-resolution Rayleigh wave tomography: a test of the conductive cooling model. Earth Planet. Sci. Lett. 278 (1–2), 96–106.
- Heiken, G., Goff, F., Gardner, J.N., Baldridge, W.S., Hulen, J.B., Nielson, D.L., Vaniman, D., 1990. The Valles/Toledo Caldera complex, Jemez Volcanic Field, New Mexico. Annu. Rev. Earth Planet. Sci. 18 (1), 27–53.
- Herrmann, R.B., Benz, H., Ammon, C.J., 2011. Monitoring the earthquake source process in North America. Bull. Seismol. Soc. Am. 101 (6), 2609–2625.
- Hildreth, W., 2004. Volcanological perspectives on Long Valley, Mammoth Mountain, and Mono Craters: several contiguous but discrete systems. J. Volcanol. Geotherm. Res. 136 (3–4), 169–198.
- Hildreth, W., 2017. Fluid-driven uplift at Long Valley Caldera, California: geologic perspectives. J. Volcanol. Geotherm. Res. 341, 269–286.
- Hildreth, W., Wilson, C.J., 2007. Compositional zoning of the Bishop Tuff. J. Petrol. 48 (5), 951–999.
- Hill, D.P., Kissling, E., Luetgert, J.H., Kradolfer, U., 1985. Constraints on the upper crustal structure of the Long Valley-Mono Craters volcanic complex, eastern California, from seismic refraction measurements. Journal of Geophysical Research: Solid Earth 90 (B13), 11135–11150.
- Hotovec-Ellis, A. J., Shelly, D. R., Hill, D. P., Pitt, A. M., Dawson, P. B., & Chouet, B. A. (2018). Deep fluid pathways beneath Mammoth Mountain, California, illuminated by migrating earthquake swarms. Science advances, 4(8), eaat5258.
- House, L., Hartse, H., 1995. Seismicity and Faults in Northern New Mexico. Geology of the Santa Fe Region, New Mexico, pp. 135–137.
- Huang, H.H., Lin, F.C., Schmandt, B., Farrell, J., Smith, R.B., Tsai, V.C., 2015. The Yellowstone magmatic system from the mantle plume to the upper crust. Science 348 (6236), 773–776.
- Humphreys, E.D., Dueker, K.G., 1994. Physical state of the western US upper mantle. Journal of Geophysical Research: Solid Earth 99 (B5), 9635–9650.
- Husen, S., Smith, R.B., Waite, G.P., 2004. Evidence for gas and magmatic sources beneath the Yellowstone volcanic field from seismic tomographic imaging. J. Volcanol. Geotherm. Res. 131 (3–4), 397–410.
- Izett, G.A., Obradovich, J.D., 1994. 40Ar/39Ar age constraints for the Jaramillo Normal Subchron and the Matuyama-Brunhes geomagnetic boundary. Journal of Geophysical Research: Solid Earth 99 (B2), 2925–2934.
- Jackson, I., Faul, U.H., 2010. Grain size-sensitive viscoelastic relaxation in olivine: Towards a robust laboratory-based model for seismological application. Phys. Earth Planet. Inter. 183 (1–2), 151–163.
- James, D.E., Fouch, M.J., Carlson, R.W., Roth, J.B., 2011. Slab fragmentation, edge flow and the origin of the Yellowstone hotspot track. Earth Planet. Sci. Lett. 311 (1–2), 124–135.
- Jaxybulatov, K., Shapiro, N.M., Koulakov, I., Mordret, A., Landès, M., Sens-Schönfelder, C., 2014. A large magmatic sill complex beneath the Toba caldera. Science 346 (6209), 617–619.
- Jiang, C., Schmandt, B., Farrell, J., Lin, F.C., Ward, K.M., 2018a. Seismically anisotropic magma reservoirs underlying silicic calderas. Geology 46 (8), 727–730.

- Jiang, C., Schmandt, B., Hansen, S.M., Dougherty, S.L., Clayton, R.W., Farrell, J., Lin, F.C., 2018b. Rayleigh and S wave tomography constraints on subduction termination and lithospheric foundering in Central California. Earth Planet. Sci. Lett. 488, 14–26.
- Julian, B. R., & Foulger, G. R. (2010). Time-dependent seismic tomography. Geophys. J. Int., 182(3), 1327–1338.
- Karakas, O., Degruyter, W., Bachmann, O., Dufek, J., 2017. Lifetime and size of shallow magma bodies controlled by crustal-scale magmatism. Nat. Geosci. 10 (6), 446.
- Karlstrom, K.E., Humphreys, E.D., 1998. Persistent influence of Proterozoic accretionary boundaries in the tectonic evolution of southwestern North America: Interaction of cratonic grain and mantle modification events. Rocky Mountain Geology 33 (2), 161–179.
- Kennedy, B., Wilcock, J., Stix, J., 2012. Caldera resurgence during magma replenishment and rejuvenation at Valles and Lake City calderas. Bull. Volcanol. 74 (8), 1833–1847.
- Kiser, E., Palomeras, I., Levander, A., Zelt, C., Harder, S., Schmandt, B., Hansen, S.M., Creager, K.C., Ulberg, C., 2016. Magma reservoirs from the upper crust to the Moho inferred from high-resolution Vp and Vs models beneath Mount St. Helens, Washington State, USA. Geology 44 (6), 411–414.
- Kiser, E., Levander, A., Zelt, C., Schmandt, B., Hansen, S., 2018. Focusing of melt near the top of the Mount St. Helens (USA) magma reservoir and its relationship to major volcanic eruptions. Geology 46 (9), 775–778.
- Kissling, E., 1988. Geotomography with local earthquake data. Rev. Geophys. 26 (4), 659-698
- Kohlstedt, D.L., Holtzman, B.K., 2009. Shearing melt out of the Earth: an experimentalist's perspective on the influence of deformation on melt extraction. Annu. Rev. Earth Planet. Sci. 37. 561–593.
- Koulakov, I., Yudistira, T., Luehr, B.G., 2009. P, S velocity and VP/VS ratio beneath the Toba caldera complex (Northern Sumatra) from local earthquake tomography. Geophys. I. Int. 177 (3), 1121–1139
- Koulakov, I., Gordeev, E.I., Dobretsov, N.L., Vernikovsky, V.A., Senyukov, S., Jakovlev, A., Jaxybulatov, K., 2013. Rapid changes in magma storage beneath the Klyuchevskoy group of volcanoes inferred from time-dependent seismic tomography. J. Volcanol. Geotherm. Res. 263, 75–91.
- Kreemer, C., Blewitt, G., Klein, E.C., 2014. A geodetic plate motion and Global Strain Rate Model. Geochem. Geophys. Geosyst. 15 (10), 3849–3889.
- Krischer, L., Fichtner, A., Žukauskaite, S., Igel, H., 2015. Large-scale seismic inversion framework. Seismol. Res. Lett. 86 (4), 1198–1207.
- Kuntz, M.A., Skipp, B., Champion, D.E., Gans, P.B., Van Sistine, D.P., Snyders, S.R., 2007. Geologic Map of the Craters of the Moon 30'x 60'quadrangle. Idaho, USGS.
- Landman, R.L., Flowers, R.M., 2013. (U-Th)/he thermochronologic constraints on the evolution of the northern Rio Grande Rift, Gore Range, Colorado, and implications for rift propagation models. Geosphere 9 (1), 170–187.
- Lane, C.S., Chorn, B.T., Johnson, T.C., 2013. Ash from the Toba supereruption in Lake Malawi shows no volcanic winter in East Africa at 75 ka. Proc. Natl. Acad. Sci. 110 (20), 8025–8029.
- Lee, E.J., Chen, P., Jordan, T.H., Maechling, P.B., Denolle, M.A., Beroza, G.C., 2014. Full-3-D tomography for crustal structure in southern California based on the scattering-integral and the adjoint-wavefield methods. Journal of Geophysical Research: Solid Earth 119 (8), 6421–6451.
- Lees, J.M., 2007. Seismic tomography of magmatic systems. J. Volcanol. Geotherm. Res. 167 (1–4), 37–56.
- Lekić, V., Fischer, K.M., 2014. Contrasting lithospheric signatures across the western United States revealed by Sp receiver functions. Earth Planet. Sci. Lett. 402, 90–98.
- de León, A.C., Schmitt, A.K., 2019. Reconciling Li and O diffusion in zircon with protracted magmatic crystal residence. Contrib. Mineral. Petrol. 174 (4), 28.
- Leonard, T., Liu, L., 2016. The role of a mantle plume in the formation of Yellowstone volcanism. Geophys. Res. Lett. 43 (3), 1132–1139.
- Lesne, P., Kohn, S.C., Blundy, J., Witham, F., Botcharnikov, R.E., Behrens, H., 2011. Experimental simulation of closed-system degassing in the system basalt–H2O–CO2–S–Cl. J. Petrol. 52 (9), 1737–1762.
- Levander, A., Miller, M.S., 2012. Evolutionary aspects of lithosphere discontinuity structure in the western US. Geochem. Geophys. Geosyst. 13 (7).
- Levandowski, W., Jones, C.H., Shen, W., Ritzwoller, M.H., Schulte-Pelkum, V., 2014. Origins of topography in the western US: Mapping crustal and upper mantle density variations using a uniform seismic velocity model. Journal of Geophysical Research: Solid Earth 119 (3), 2375–2396.
- Li, J., Lin, F.C., Allam, A., Ben-Zion, Y., Liu, Z., Schuster, G., 2019. Wave equation dispersion inversion of surface waves recorded on irregular topography. Geophys. J. Int. 217 (1), 346–360.
- Lin, F.C., Moschetti, M.P., Ritzwoller, M.H., 2008. Surface wave tomography of the western United States from ambient seismic noise: Rayleigh and love wave phase velocity maps. Geophys. J. Int. 173 (1), 281–298.
- Lin, F.C., Ritzwoller, M.H., Snieder, R., 2009. Eikonal tomography: surface wave tomography by phase front tracking across a regional broad-band seismic array. Geophys. J. Int. 177 (3), 1091–1110.
- Lin, F.C., Li, D., Clayton, R.W., Hollis, D., 2013. High-resolution 3D shallow crustal structure in Long Beach, California: application of ambient noise tomography on a dense seismic array. Geophysics 78 (4), 045–056.
- Lin, G., 2015. Seismic velocity structure and earthquake relocation for the magmatic system beneath Long Valley Caldera, eastern California. J. Volcanol. Geotherm. Res. 296, 19–30.
- Lin, G., Thurber, C.H., Zhang, H., Hauksson, E., Shearer, P.M., Waldhauser, F., ... Hardebeck, J., 2010. A California statewide three-dimensional seismic velocity model from both absolute and differential times. Bull. Seismol. Soc. Am. 100 (1), 225–240.
- Lipman, P.W., Mehnert, H.H., 1980. Potassium-Argon Ages from the Mount Taylor Volcanic Field. US Government Printing Office, New Mexico.

- Liu, K., Levander, A., 2012. Three-dimensional Kirchhoff-approximate generalized Radon transform imaging using teleseismic P-to-S scattered waves. Geophys. J. Int. 192 (3), 1196–1216.
- Liu, Y., Niu, F., Chen, M., Yang, W., 2017. 3-D crustal and uppermost mantle structure beneath NE China revealed by ambient noise adjoint tomography. Earth Planet. Sci. Lett. 461. 20–29.
- Lowry, A.R., Ribe, N.M., Smith, R.B., 2000. Dynamic elevation of the Cordillera, western United States. Journal of Geophysical Research: Solid Earth 105 (B10), 23371–23390.
- Lynner, C., Beck, S.L., Zandt, G., Porritt, R.W., Lin, F.C., Eilon, Z.C., 2018. Midcrustal deformation in the Central Andes constrained by radial anisotropy. Journal of Geophysical Research: Solid Earth 123 (6), 4798–4813.
- Mann, M.E., Abers, G.A., Crosbie, K., Creager, K., Ulberg, C., Moran, S., Rondenay, S., 2019. Imaging subduction beneath Mount St. Helens: Implications for Slab Dehydration and Magma Transport. Letters, Geophysical Research.
- Marsh, B.D., 1981. On the crystallinity, probability of occurrence, and rheology of lava and magma. Contrib. Mineral. Petrol. 78 (1), 85–98.
- Masterlark, T., Haney, M., Dickinson, H., Fournier, T., Searcy, C., 2010. Rheologic and structural controls on the deformation of Okmok volcano, Alaska: FEMs, InSAR, and ambient noise tomography. Journal of Geophysical Research: Solid Earth 115 (B2).
- Matthews, N.E., Vazquez, J.A., Calvert, A.T., 2015. Age of the Lava Creek supereruption and magma chamber assembly at Yellowstone based on 40Ar/39Ar and U-Pb dating of sanidine and zircon crystals. Geochem. Geophys. Geosyst. 16 (8), 2508–2528.
- Mavko, G.M., 1980. Velocity and attenuation in partially molten rocks. Journal of Geophysical Research: Solid Earth 85 (B10), 5173–5189.
- McCarthy, C., Takei, Y., 2011. Anelasticity and viscosity of partially molten rock analogue: toward seismic detection of small quantities of melt. Geophys. Res. Lett. 38 (18).
- Metz, J.M., Mahood, G.A., 1991. Development of the Long Valley, California, magma chamber recorded in precaldera rhyolite lavas of Glass Mountain. Contrib. Mineral. Petrol. 106 (3). 379–397.
- Montgomery-Brown, E.K., Wicks, C.W., Cervelli, P.F., Langbein, J.O., Svarc, J.L., Shelly, D.R., Hill, D.P., Lisowski, M., 2015. Renewed inflation of Long Valley Caldera, California (2011 to 2014). Geophys. Res. Lett. 42 (13), 5250–5257.
- Mordret, A., Rivet, D., Landès, M., Shapiro, N.M., 2015. Three-dimensional shear velocity anisotropic model of Piton de la Fournaise Volcano (La Réunion Island) from ambient seismic noise. Journal of Geophysical Research: Solid Earth 120 (1), 406–427.
- Moschetti, M.P., Ritzwoller, M.H., Lin, F., Yang, Y., 2010. Seismic evidence for widespread western-US deep-crustal deformation caused by extension. Nature 464 (7290), 885.
- Myers, M.L., Wallace, P.J., Wilson, C.J., Morter, B.K., Swallow, E.J., 2016. Prolonged ascent and episodic venting of discrete magma batches at the onset of the Huckleberry Ridge supereruption, Yellowstone. Earth Planet. Sci. Lett. 451, 285–297.
- Nakai, J.S., Sheehan, A.F., Bilek, S.L., 2017. Seismicity of the rocky mountains and Rio Grande Rift from the EarthScope Transportable Array and CREST temporary seismic networks, 2008–2010. Journal of Geophysical Research: Solid Earth 122 (3), 2173–2192.
- Nakata, N., Shelly, D.R., 2018. Imaging a crustal low-velocity layer using reflected seismic waves from the 2014 earthquake swarm at Long Valley Caldera, California: the magmatic system roof? Geophys. Res. Lett. 45 (8), 3481–3488.
- Nelson, P.L., Grand, S.P., 2018. Lower-mantle plume beneath the Yellowstone hotspot revealed by core waves. Nat. Geosci. 11 (4), 280.
- Newhall, C., Self, S., Robock, A., 2018. Anticipating future Volcanic Explosivity Index (VEI) 7 eruptions and their chilling impacts. Geosphere 14 (2), 572–603.
- Newhall, C.G., Self, S., 1982. The volcanic explosivity index (VEI) an estimate of explosive magnitude for historical volcanism. Journal of Geophysical Research: Oceans 87 (C2), 1231–1238.
- Obrebski, M., Allen, R.M., Xue, M., Hung, S.H., 2010. Slab-plume interaction beneath the Pacific Northwest. Geophys. Res. Lett. 37 (14).
- Obrebski, M., Allen, R.M., Pollitz, F., Hung, S.H., 2011. Lithosphere–asthenosphere interaction beneath the western United States from the joint inversion of body-wave traveltimes and surface-wave phase velocities. Geophys. J. Int. 185 (2), 1003–1021.
- Olsen, K.H., Baldridge, W.S., Callender, J.F., 1987. Rio Grande rift: an overview. Tectonophysics 143 (1–3), 119–139.
- Oppenheimer, C., 2003. Climatic, environmental and human consequences of the largest known historic eruption: Tambora volcano (Indonesia) 1815. Prog. Phys. Geogr. 27 (2), 230–259.
- Phillips, E.H., Goff, F., Kyle, P.R., McIntosh, W.C., Dunbar, N.W., Gardner, J.N., 2007. The 40Ar/39Ar age constraints on the duration of resurgence at the Valles caldera, New Mexico. Journal of Geophysical Research: Solid Earth 112 (B8).
- Pierce, K.L., Morgan, L.A., 2009. Is the track of the Yellowstone hotspot driven by a deep mantle plume?—Review of volcanism, faulting, and uplift in light of new data. J. Volcanol. Geotherm. Res. 188 (1–3), 1–25.
- Ping, P., Chu, R., Chong, J., Ni, S., Zhang, Y., 2018. Insight into large-scale topography on analysis of high-frequency Rayleigh waves. J. Appl. Geophys. 150, 1–10.
- Plank, T., Forsyth, D.W., 2016. Thermal structure and melting conditions in the mantle beneath the Basin and Range province from seismology and petrology. Geochem. Geophys. Geosyst. 17 (4), 1312–1338.
- Poppeliers, C., & Pavlis, G. L. (2003). Three-dimensional, prestack, plane wave migration of teleseismic P-to-S converted phases: 1. Theory. *Journal of Geophysical Research: Solid Earth*, 108(B2).
- Postma, G.W., 1955. Wave propagation in a stratified medium. Geophysics 20 (4), 780–806.
- Potter, K.E., Champion, D.E., Duncan, R.A., Shervais, J.W., 2019. Volcanic stratigraphy and age model of the Kimama deep borehole (Project Hotspot): evidence for 5.8 million years of continuous basalt volcanism, Central Snake River Plain. Idaho. *Geosphere*. 15 (3), 736–758.

- Pribnow, D.F., Schütze, C., Hurter, S.J., Flechsig, C., Sass, J.H., 2003. Fluid flow in the resurgent dome of Long Valley Caldera: implications from thermal data and deep electrical sounding. J. Volcanol. Geotherm. Res. 127 (3–4), 329–345.
- Pritchard, M.E., Gregg, P.M., 2016. Geophysical evidence for silicic crustal melt in the continents: where, what kind, and how much? Elements 12 (2), 121–127.
- Pritchard, M.E., de Silva, S.L., Michelfelder, G., Zandt, G., McNutt, S.R., Gottsmann, J., West, M.E., Blundy, J., Christensen, D.H., Finnegan, N.J., Minaya, E., 2018. Synthesis: PLUTONS: investigating the relationship between pluton growth and volcanism in the Central Andes. Geosphere 14 (3), 954–982.
- Prudencio, J., Manga, M., Taira, T., 2018. Subsurface structure of Long Valley Caldera imaged with seismic scattering and intrinsic attenuation. Journal of Geophysical Research: Solid Earth 123 (7), 5987–5999.
- Puskas, C.M., Smith, R.B., Meertens, C.M., Chang, W.L., 2007. Crustal deformation of the Yellowstone–Snake River Plain volcano-tectonic system: Campaign and continuous GPS observations, 1987–2004. Journal of Geophysical Research: Solid Earth 112 (B3).
- Pyle, D.M., 1995. Mass and energy budgets of explosive volcanic eruptions. Geophys. Res. Lett. 22 (5), 563–566.
- Pyle, D. M. (2015). Sizes of volcanic eruptions. In *The encyclopedia of volcanoes* (pp. 257–264). Academic Press.
- Reneau, S.L., Gardner, J.N., Forman, S.L., 1996. New evidence for the age of the youngest eruptions in the Valles caldera, New Mexico. Geology 24 (1), 7–10.
- Reuber, G.S., Kaus, B.J.P., Popov, A.A., Baumann, T.S., 2018. Unraveling the physics of the Yellowstone magmatic system using geodynamic simulations. Front. Earth Sci. 6, 117.
- Ricketts, J.W., Kelley, S.A., Karlstrom, K.E., Schmandt, B., Donahue, M.S., van Wijk, J., 2016. Synchronous opening of the Rio Grande rift along its entire length at 25–10 Ma supported by apatite (U-Th)/he and fission-track thermochronology, and evaluation of possible driving mechanisms. GSA Bull. 128 (3–4), 397–424.
- Rigo, A., Adam, C., Grégoire, M., Gerbault, M., Meyer, R., Rabinowicz, M., Fontaine, F., Bonvalot, S., 2015. Insights for the melt migration, the volcanic activity and the ultrafast lithosphere delamination related to the Yellowstone plume (Western USA). Geophys. J. Int. 203 (2), 1274–1301.
- Rivera, T.A., Schmitz, M.D., Crowley, J.L., Storey, M., 2014. Rapid magma evolution constrained by zircon petrochronology and 40Ar/39Ar sanidine ages for the Huckleberry Ridge Tuff, Yellowstone, USA. Geology 42 (8), 643–646.
- Rivera, T.A., Schmitz, M.D., Jicha, B.R., Crowley, J.L., 2016. Zircon petrochronology and 40Ar/39Ar sanidine dates for the Mesa Falls Tuff: Crystal-scale records of magmatic evolution and the short lifespan of a large Yellowstone magma chamber. J. Petrol. 57 (9), 1677–1704.
- Roberge, J., Wallace, P.J., Kent, A.J.R., 2013. Magmatic processes in the Bishop Tuff rhyolitic magma based on trace elements in melt inclusions and pumice matrix glass. Contrib. Mineral. Petrol. 165 (2), 237–257.
- Rougier, J., Sparks, R.S.J., Cashman, K.V., Brown, S.K., 2018. The global magnitude–frequency relationship for large explosive volcanic eruptions. Earth Planet. Sci. Lett. 482, 621–629.
- Rubin, A.E., Cooper, K.M., Till, C.B., Kent, A.J., Costa, F., Bose, M., Gravley, D., Deering, C., Cole, J., 2017. Rapid cooling and cold storage in a silicic magma reservoir recorded in individual crystals. Science 356 (6343), 1154–1156.
- Sabra, K.G., Gerstoft, P., Roux, P., Kuperman, W.A., Fehler, M.C., 2005. Extracting time-domain Green's function estimates from ambient seismic noise. Geophys. Res. Lett. 32 (3).
- Sanders, C.O., 1984. Location and configuration of magma bodies beneath Long Valley, California, determined from anomalous earthquake signals. Journal of Geophysical Research: Solid Earth 89 (B10), 8287–8302.
- Schellart, W.P., Stegman, D.R., Farrington, R.J., Freeman, J., Moresi, L., 2010. Cenozoic tectonics of western North America controlled by evolving width of Farallon slab. Science 329 (5989), 316–319.
- Scheu, B., Kern, H., Spieler, O., Dingwell, D.B., 2006. Temperature dependence of elastic Pand S-wave velocities in porous Mt. Unzen dacite. J. Volcanol. Geotherm. Res. 153 (1–2) 136–147
- Schilling, F.R., Sinogeikin, S.V., Hauser, M., Bass, J.D., 2003. Elastic properties of model basaltic melt compositions at high temperatures. Journal of Geophysical Research: Solid Earth 108 (B6).
- Schlue, J.W., Aster, R.C., Meyer, R.P., 1996. A lower crustal extension to a midcrustal magma body in the Rio Grande Rift, New Mexico. Journal of Geophysical Research: Solid Earth 101 (B11), 25283–25291.
- Schmandt, B., Clayton, R.W., 2013. Analysis of teleseismic P waves with a 5200-station array in Long Beach, California: evidence for an abrupt boundary to Inner Borderland rifting. Journal of Geophysical Research: Solid Earth 118 (10), 5320–5338.
- Schmandt, B., Humphreys, E., 2010. Complex subduction and small-scale convection revealed by body-wave tomography of the western United States upper mantle. Earth Planet. Sci. Lett. 297 (3–4), 435–445.
- Schmandt, B., Lin, F.C., 2014. P and S wave tomography of the mantle beneath the United States. Geophys. Res. Lett. 41 (18), 6342–6349.
- Schmandt, B., Dueker, K., Humphreys, E., Hansen, S., 2012. Hot mantle upwelling across the 660 beneath Yellowstone. Earth Planet. Sci. Lett. 331, 224–236.
- Schmeling, H., 1985. Numerical models on the influence of partial melt on elastic, anelastic and electric properties of rocks. Part I: elasticity and anelasticity. Phys. Earth Planet. Inter. 41 (1), 34–57.
- Schutt, D.L., Dueker, K., 2008. Temperature of the plume layer beneath the Yellowstone hotspot. Geology 36 (8), 623–626.
- Schutt, D.L., Lesher, C.E., 2006. Effects of melt depletion on the density and seismic velocity of garnet and spinel lherzolite. Journal of Geophysical Research: Solid Earth 111 (B5).
- Schutt, D.L., Dueker, K., Yuan, H., 2008. Crust and upper mantle velocity structure of the Yellowstone hot spot and surroundings. Journal of Geophysical Research: Solid Earth 113 (B3).

- Seats, K.J., Lawrence, J.F., 2014. The seismic structure beneath the Yellowstone Volcano Field from ambient seismic noise. Geophys. Res. Lett. 41 (23), 8277–8282.
- Seccia, D., Chiarabba, C., De Gori, P., Bianchi, I., Hill, D.P., 2011. Evidence for the contemporary magmatic system beneath Long Valley Caldera from local earthquake tomography and receiver function analysis. Journal of Geophysical Research: Solid Earth 116 (B12).
- Shamloo, H.I., Till, C.B., 2019. Decadal transition from quiescence to supereruption: petrologic investigation of the Lava Creek Tuff, Yellowstone Caldera, WY. Contrib. Mineral. Petrol. 174 (4). 32.
- Shang, X., Hoop, M.V., Hilst, R.D., 2012. Beyond receiver functions: Passive source reverse time migration and inverse scattering of converted waves. Geophys. Res. Lett. 39 (15)
- Shapiro, N.M., Campillo, M., 2004. Emergence of broadband Rayleigh waves from correlations of the ambient seismic noise. Geophys. Res. Lett. 31 (7).
- Shelly, D.R., Hill, D.P., 2011. Migrating swarms of brittle-failure earthquakes in the lower crust beneath Mammoth Mountain, California. Geophys. Res. Lett. 38 (20).
- Shelly, D.R., Hill, D.P., Massin, F., Farrell, J., Smith, R.B., Taira, T.A., 2013. A fluid-driven earthquake swarm on the margin of the Yellowstone caldera. Journal of Geophysical Research: Solid Earth 118 (9), 4872–4886.
- Shen, W., Ritzwoller, M.H., 2016. Crustal and uppermost mantle structure beneath the United States. Journal of Geophysical Research: Solid Earth 121 (6), 4306–4342.
- de Silva, S.L., Gregg, P.M., 2014. Thermomechanical feedbacks in magmatic systems: Implications for growth, longevity, and evolution of large caldera-forming magma reservoirs and their supereruptions. J. Volcanol. Geotherm. Res. 282, 77–91.
- Singer, B.S., Jicha, B.R., Condon, D.J., Macho, A.S., Hoffman, K.A., Dierkhising, J., Brown, M.C., Feinberg, J.M., Kidane, T., 2014. Precise ages of the Réunion event and Huckleberry Ridge excursion: Episodic clustering of geomagnetic instabilities and the dynamics of flow within the outer core. Earth Planet. Sci. Lett. 405, 25–38.
- Slack, P.D., Davis, P.M., Baldridge, W.S., Olsen, K.H., Glahn, A., Achauer, U., Spence, W., 1996. The upper mantle structure of the Central Rio Grande rift region from teleseismic P and S wave travel time delays and attenuation. Journal of Geophysical Research: Solid Earth 101 (B7), 16003–16023.
- Smith, D.A., Milbert, D.G., 1999. The GEOID96 high-resolution GEOID height model for the United States. J. Geod. 73 (5), 219–236.
- Smith, E.I., Jacobs, Z., Johnsen, R., Ren, M., Fisher, E.C., Oestmo, S., Wilkins, J., Harris, J.A., Karkanas, P., Fitch, S., Ciravolo, A., 2018. Humans thrived in South Africa through the Toba eruption about 74,000 years ago. Nature 555 (7697), 511.
- Smith, R. B., & Braile, L. W. (1994). The yellowstone hotspot. J. Volcanol. Geotherm. Res., 61(3–4), 121–187.
- Smith, R.B., Sbar, M.L., 1974. Contemporary tectonics and seismicity of the western United States with emphasis on the Intermountain Seismic Belt. Geol. Soc. Am. Bull. 85 (8), 1205–1218.
- Smith, R.B., Jordan, M., Steinberger, B., Puskas, C.M., Farrell, J., Waite, G.P., Husen, S., Chang, W.L., O'Connell, R., 2009. Geodynamics of the Yellowstone hotspot and mantle plume: Seismic and GPS imaging, kinematics, and mantle flow. J. Volcanol. Geotherm. Res. 188 (1–3), 26–56.
- Snieder, R., 1986. The influence of topography on the propagation and scattering of surface waves. Phys. Earth Planet. Inter. 44 (3), 226–241.
- Solano, J.M.S., Jackson, M.D., Sparks, R.S.J., Blundy, J.D., Annen, C., 2012. Melt segregation in deep crustal hot zones: a mechanism for chemical differentiation, crustal assimilation and the formation of evolved magmas. J. Petrol. 53 (10), 1999–2026.
- Spell, T.L., McDougall, I., Doulgeris, A.P., 1996. Cerro Toledo Rhyolite, Jemez Volcanic Field, New Mexico: 40Ar/39Ar geochronology of eruptions between two caldera-forming events. Geol. Soc. Am. Bull. 108 (12), 1549–1566.
- Stachnik, J.C., Dueker, K., Schutt, D.L., Yuan, H., 2008. Imaging Yellowstone plume-lithosphere interactions from inversion of ballistic and diffusive Rayleigh wave dispersion and crustal thickness data. Geochem. Geophys. Geosyst. 9 (6).
- Steck, L.K., Prothero, W.A., 1994. Crustal structure beneath Long Valley caldera from modeling of teleseismic P wave polarizations and Ps converted waves. Journal of Geophysical Research: Solid Earth 99 (B4), 6881–6898.
- Steck, L.K., Thurber, C.H., Fehler, M.C., Lutter, W.J., Roberts, P.M., Baldridge, W.S., Stafford, D.G., Sessions, R., 1998. Crust and upper mantle P wave velocity structure beneath Valles caldera, New Mexico: results from the Jemez teleseismic tomography experiment. Journal of Geophysical Research: Solid Earth 103 (B10), 24301–24320.
- Stelten, M.E., Cooper, K.M., Vazquez, J.A., Calvert, A.T., Glessner, J.J., 2015. Mechanisms and timescales of generating eruptible rhyolitic magmas at Yellowstone caldera from zircon and sanidine geochronology and geochemistry. J. Petrol. 56 (8), 1607–1642.
- Suppe, J., Powell, C., Berry, R., 1975. Regional topography, seismicity, Quaternary volcanism, and the present-day tectonics of the western United States. Am. J. Sci. 275A, 397–436
- Swallow, E.J., Wilson, C.J., Myers, M.L., Wallace, P.J., Collins, K.S., Smith, E.G., 2018. Evacuation of multiple magma bodies and the onset of caldera collapse in a supereruption, captured in glass and mineral compositions. Contrib. Mineral. Petrol. 173 (4), 33.
- Taira, T., Smith, R.B., Chang, W.L., 2010. Seismic evidence for dilatational source deformations accompanying the 2004–2008 Yellowstone accelerated uplift episode. Journal of Geophysical Research: Solid Earth (B2), 115.
- Takei, Y., 2002. Effect of pore geometry on Vp/Vs: from equilibrium geometry to crack. Journal of Geophysical Research: Solid Earth 107 (B2), ECV–6.
- Takei, Y., 2017. Effects of partial melting on seismic velocity and attenuation: a new insight from experiments. Annu. Rev. Earth Planet. Sci. 45, 447–470.
- Tape, C., Liu, Q., Maggi, A., Tromp, J., 2010. Seismic tomography of the southern California crust based on spectral-element and adjoint methods. Geophys. J. Int. 180 (1), 433–462.
- Taylor, M.A.J., Singh, S.C., 2002. Composition and microstructure of magma bodies from effective medium theory. Geophys. J. Int. 149 (1), 15–21.

- Thurber, C., Zhang, H., Brocher, T., Langenheim, V., 2009. Regional three-dimensional seismic velocity model of the crust and uppermost mantle of northern California. Journal of Geophysical Research: Solid Earth 114 (B1).
- Till, C.B., Vazquez, J.A., Boyce, J.W., 2015. Months between rejuvenation and volcanic eruption at Yellowstone caldera, Wyoming, Geology 43 (8), 695–698.
- Timmreck, C., 2012. Modeling the climatic effects of large explosive volcanic eruptions. Wiley Interdiscip. Rev. Clim. Chang. 3 (6), 545–564.
- Tizzani, P., Battaglia, M., Zeni, G., Atzori, S., Berardino, P., Lanari, R., 2009. Uplift and magma intrusion at Long Valley caldera from InSAR and gravity measurements. Geology 37 (1), 63–66.
- Tramelli, A., Del Pezzo, E., Bianco, F., Boschi, E., 2006. 3D scattering image of the Campi Flegrei caldera (Southern Italy): new hints on the position of the old caldera rim. Phys. Earth Planet. Inter. 155 (3–4), 269–280.
- Virieux, J., Operto, S., 2009. An overview of full-waveform inversion in exploration geophysics. Geophysics 74 (6), WCC1–WCC26.
- Wagner, L., Forsyth, D.W., Fouch, M.J., James, D.E., 2010. Detailed three-dimensional shear wave velocity structure of the northwestern United States from Rayleigh wave tomography. Earth Planet. Sci. Lett. 299 (3–4), 273–284.
- Waite, G.P., Smith, R.B., Allen, R.M., 2006. VP and VS structure of the Yellowstone hot spot from teleseismic tomography: evidence for an upper mantle plume. Journal of Geophysical Research: Solid Earth (B4), 111.
- Walker, J. D., Bowers, T. D., Glazner, A. F., Farmer, A. L., & Carlson, R. W. (2004, May). Creation of a north American volcanic and plutonic rock database (NAVDAT). In Geological Society of America Abstracts with Programs (Vol. vol. 36, No. 4, p. 9).
- Wallace, P.J., 2005. Volatiles in subduction zone magmas: concentrations and fluxes based on melt inclusion and volcanic gas data. J. Volcanol. Geotherm. Res. 140 (1–3), 217–240.
- Wallace, P.J., Anderson Jr., A.T., Davis, A.M., 1999. Gradients in H2O, CO2, and exsolved gas in a large-volume silicic magma system: Interpreting the record preserved in melt inclusions from the Bishop Tuff. Journal of Geophysical Research: Solid Earth 104 (B9), 20097–20122.
- Ward, K.M., Zandt, G., Beck, S.L., Christensen, D.H., McFarlin, H., 2014. Seismic imaging of the magmatic underpinnings beneath the Altiplano-Puna volcanic complex from the joint inversion of surface wave dispersion and receiver functions. Earth Planet. Sci. Lett. 404. 43–53.
- Wark, D.A., Hildreth, W., Spear, F.S., Cherniak, D.J., Watson, E.B., 2007. Pre-eruption recharge of the Bishop magma system. Geology 35 (3), 235–238.
- Watanabe, T., 1993. Effects of water and melt on seismic velocities and their application to characterization of seismic reflectors. Geophys. Res. Lett. 20 (24), 2933–2936.
- Watts, K.E., Bindeman, I.N., Schmitt, A.K., 2012. Crystal scale anatomy of a dying supervolcano: an isotope and geochronology study of individual phenocrysts from voluminous rhyolites of the Yellowstone caldera. Contrib. Mineral. Petrol. 164 (1), 45–67
- Weiland, C.M., Steck, L.K., Dawson, P.B., Korneev, V.A., 1995. Nonlinear teleseismic tomography at Long Valley Caldera, using three-dimensional minimum travel time ray tracing. J. Geophys. Res. Solid Earth 100 (B10), 20379–20390.

- Wespestad, C.E., Thurber, C.H., Andersen, N.L., Singer, B.S., Cardona, C., Zeng, X., Bennington, N.L., Keranen, K., Peterson, D.E., Cordell, D., Unsworth, M., 2019. Magma Reservoir Below Laguna del Maule Volcanic Field, Chile, Imaged with Surface-Wave Tomography. Journal of Geophysical Research: Solid Earth 124 (3), 2858–2872.
- West, M., Ni, J., Baldridge, W.S., Wilson, D., Aster, R., Gao, W., Grand, S., 2004. Crust and upper mantle shear wave structure of the Southwest United States: Implications for rifting and support for high elevation. Journal of Geophysical Research: Solid Earth 109 (B3).
- Wilson, C.J., Morgan, D.J., Charlier, B.L., Barker, S.J., 2017. Comment on "Rapid cooling and cold storage in a silicic magma reservoir recorded in individual crystals". Science 358 (6370) eaan8429
- Wolff, J.A., Gardner, J.N., 1995. Is the Valles caldera entering a new cycle of activity? Geology 23 (5), 411–414.
- Wolff, J.A., Ramos, F.C., 2013. Processes in caldera-forming high-silica rhyolite magma: Rb-Sr and Pb isotope systematics of the Otowi Member of the Bandelier Tuff, Valles Caldera, New Mexico, USA. J. Petrol. 55 (2), 345–375.
- Woltering, M., Johnson, T.C., Werne, J.P., Schouten, S., Damsté, J.S.S., 2011. Late Pleistocene temperature history of Southeast Africa: a TEX86 temperature record from Lake Malawi. Palaeogeogr. Palaeoclimatol. Palaeoecol. 303 (1–4), 93–102.
- Wotzlaw, J.F., Bindeman, I.N., Stern, R.A., D'Abzac, F.X., Schaltegger, U., 2015. Rapid heterogeneous assembly of multiple magma reservoirs prior to Yellowstone supereruptions. Sci. Rep. 5, 14026.
- Yang, Y., Forsyth, D.W., 2006. Rayleigh wave phase velocities, small-scale convection, and azimuthal anisotropy beneath southern. California. *Journal of Geophysical Research: Solid Earth* (B7), 111.
- Yuan, Y.O., Simons, F.J., 2014. Multiscale adjoint waveform-difference tomography using wavelets. Geophysics 79 (3), WA79–WA95.
- Yuan, Y.O., Simons, F.J., Bozdağ, E., 2015. Multiscale adjoint waveform tomography for surface and body waves. Geophysics 80 (5), R281–R302.
- Zandomeneghi, D., Aster, R., Kyle, P., Barclay, A., Chaput, J., Knox, H., 2013. Internal structure of Erebus volcano, Antarctica imaged by high-resolution active-source seismic tomography and coda interferometry. Journal of Geophysical Research: Solid Earth 118 (3), 1067–1078.
- Zhou, Y., 2018. Anomalous mantle transition zone beneath the Yellowstone hotspot track. Nat. Geosci. 11 (6), 449.
- Zhou, Q., Liu, L., Hu, J., 2018. Western US volcanism due to intruding oceanic mantle driven by ancient Farallon slabs. Nat. Geosci. 11 (1), 70.
- Zimmerer, M.J., Lafferty, J., Coble, M.A., 2016. The eruptive and magmatic history of the youngest pulse of volcanism at the Valles caldera: Implications for successfully dating late Quaternary eruptions. J. Volcanol. Geotherm. Res. 310, 50–57.
- Zucca, J.J., Kasameyer, P.W., Mills Jr., J.M., 1987. Observation of a reflection from the base of a magma chamber in Long Valley caldera. California. *Bulletin of the Seismological Society of America* 77 (5), 1674–1687.